

Temperature and Density in the Foot Points of the Molecular Loops in the Galactic Center; Analysis of Multi-J Transitions of $^{12}\text{CO}(J=1-0, 3-2, 4-3, 7-6)$, $^{13}\text{CO}(J=1-0)$ and $\text{C}^{18}\text{O}(J=1-0)$

Kazufumi TORII,¹ Natsuko KUDO,¹ Motosuji FUJISHITA,¹ Tokuichi KAWASE,¹
 Takeshi OKUDA,¹ Hiroaki YAMAMOTO,¹ Akiko KAWAMURA,¹ Norikazu MIZUNO,²
 Toshikazu ONISHI,³ Mami MACHIDA,¹ Kunio TAKAHASHI,⁴ Satoshi NOZAWA,⁵
 Ryoji MATSUMOTO,⁶ Jürgen OTT,⁷ Kunihiro TANAKA,⁸ Nobuyuki YAMAGUCHI,⁹
 Hajime EZAWA,⁹ Jürgen STUTZKI,¹⁰ Uli KLEIN,¹¹ Frank BERTOLDI,¹¹
 Koo BON-CHUL,¹² Leonardo BRONFMAN,¹³ Michael BURTON,¹⁴ Arnold BENZ,¹⁵
 Hideo OGAWA,³ and Yasuo FUKUI¹

¹*Department of Astrophysics, Nagoya University, Furo-cho, Chikusa-ku, Nagoya, Aichi 464-8602*

²*National Astronomical Observatory of Japan, Osawa, Mitaka, Tokyo 181-8588*

³*Department of Physical Science, Osaka prefecture University, Sakai, Osaka 599-8531*

⁴*Japan Agency for Marine-Earth Science and Technology, Kanazawa-ku, Yokohama, Kanagawa 236-0001, Japan*

⁵*Department of Science, Ibaraki University, 2-1-1 Bunkyo, Mito, Ibaraki 310-8512*

⁶*Faculty of Science, Chiba University, Inage-ku, Chiba 263-8522*

⁷*National Radio Astronomy Observatory, 520 Edgemont Road, Charlottesville, VA 22903*

⁸*Institute of Science and Technology, Keio University, 4-14-1 Hiyoshi, Yokohama, Kanagawa 223-8522*

⁹*Nobeyama Radio Observatory, National Astronomical Observatory of Japan, Minamimaki, Minamisaku, Nagano 384-1305*

¹⁰*KOSMA, I. Physikalisches Institut, Universität zu Köln, Zùlpicher Straße 77, 50937 Köln, Germany*

¹¹*Radioastronomisches Institut der Universität Bonn, Auf dem Hügel 71, 53121 Bonn, Germany*

¹²*Department of Physics and Astronomy, Seoul National University, Seoul 151-742, Korea*

¹³*Departamento de Astronomía, Universidad de Chile, Casilla 36-D, Santiago, Chile*

¹⁴*School of Physics, University of New South Wales, Sydney 2052, NSW, Australia*

¹⁵*Institute of Astronomy, ETH Zurich, 8093 Zurich, Switzerland*

torii@a.phys.nagoya-u.ac.jp, fukui@a.phys.nagoya-u.ac.jp

(Received 2009 April 3; accepted 0 0)

Abstract

Fukui et al. (2006) discovered two molecular loops in the Galactic center and argued that the foot points of the molecular loops, two bright spots at the both loop ends, represent the gas accumulated by the falling motion along the loops, subsequent to the magnetic flotation by the Parker instability. We have carried out sensitive CO observations of the foot points toward $l = 356^\circ$ at a few pc resolution in the six rotational transitions of CO; $^{12}\text{CO}(J=1-0, 3-2, 4-3, 7-6)$, $^{13}\text{CO}(J=1-0)$ and $\text{C}^{18}\text{O}(J=1-0)$. The high resolution image of $^{12}\text{CO}(J=3-2)$ has revealed detailed distribution of the high excitation gas including a U shape, the outer boundary of which shows sharp intensity jumps accompanying strong velocity gradients. An analysis of the multi-J CO transitions shows that temperature is in a range from 30–100 K or higher and density is around $10^3\text{--}10^4\text{ cm}^{-3}$, confirming that the foot points have high temperature and density although there is no radiative heat source like high mass stars in and around the loops. We argue that the high temperature is likely due to the shock heating under C-shock condition caused by the magnetic flotation. We made a detailed comparison of the distribution obtained with theoretical numerical simulations and note that the U shape seems to be consistent with numerical simulations. We also find that the region of highest temperature of 60 K or higher inside the U shape corresponds to the spur having upward flow, additionally heated up either by magnetic reconnection or bouncing in the interaction with the narrow "neck" at the bottom of the U shape. We note these new findings further reinforce the magnetic flotation interpretation.

Key words: Radio lines: ISM—ISM: clouds—ISM: magnetic fields—magnetic loops

1. Introduction

The central molecular zone (hereafter CMZ, Morris & Serabyn 1996) is located in the inner 300 pc of the Galactic center and contains the Sgr A and Sgr B2 molecular clouds, two outstanding features in the CMZ (e.g., Scoville, Solomon & Penzias 1975; Fukui et al. 1977; Güsten & Henkel 1983). The molecular gas in the CMZ is characterized by high kinetic temperature from 30 K to 300 K (e.g., Rodríguez-Fernández et al. 2001; Hüttemeister et al. 1993; Martin et al. 2004; Oka et al. 2005; Nagai et al. 2007), and high density (10^4 cm^{-3}) (e.g., Tsuboi, Handa & Ukita 1999). The molecular gas in the CMZ also shows significant violent motions with the velocity dispersion of $1\sigma = 15\text{--}30\text{ km s}^{-1}$, much larger than those of the typical molecular clouds of $1\sigma = \text{a few km s}^{-1}$ outside the central kpc (Morris & Serabyn 1996; Güsten & Philipp 2004). It was suggested that supernova explosions may be responsible for these properties but the total star formation efficiency is too small to account for the required

frequency of OB stars (Morris & Serabyn 1996). The origin of these two peculiar properties, high temperatures and violent motions, has been puzzling since 1970's. It is important to understand the physical properties of the molecular gas that must be a key to understand star formation in the Galactic center and, consequently, the evolution of the Galaxy. There are also several molecular features with very broad velocity widths outside the CMZ including Clumps 1 and 2 (Bania 1977) and the $l = 5.5^\circ$ cloud (Bitran et al. 1997). These clouds located outside the CMZ are perhaps distributed in the central 1 kpc but have not been given as much attention as in the CMZ so far.

Recently, Fukui et al. (2006; F06) discovered loop-like molecular features, hereafter loops 1 and 2, toward $l = 355^\circ$ – 359° outside the CMZ (Figure 1) and showed that the two loops each have two foot points on the both ends; the foot points are bright molecular condensations and show broad velocity widths as large as $\sim 50 \text{ km s}^{-1}$. F06 suggested that the two loops are formed by magnetic flotation driven by the Parker instability and showed that numerical calculations of magneto-hydrodynamics (MHD) reproduce the loops successfully. This discovery is the first observational verification of the Parker's instability in the Galactic scale 40 years after the prediction by Parker (1966). In the scenario of F06, the two foot points are interpreted as the accumulated gas formed by the down-falling gas by the stellar gravity and details of such a signature has already been shown by numerical simulations by Matsumoto et al. (1988). F06 argues that the relatively strong magnetic field of 0.1–1.0 mG, which is eventually a result of the strong gravitation in the inner 1 kpc of the Galaxy, makes it possible to create the loops throughout the Galactic center.

Subsequently, Torii et al. (2009; T09 hereafter) made a detailed analysis of the NANTEN $^{12}\text{CO}(J=1-0)$ and $^{13}\text{CO}(J=1-0)$ datasets and revealed further details including helical distributions in loops 1 and 2 as well as associated HI and dust features. Fujishita et al. (2009) presented a discovery of loop 3, another magnetically floated loop, in the same direction with loops 1 and 2 in a positive velocity range. Machida et al. (2009) presented a three dimensional global MHD simulations in the central 2-kpc magnetized gas disk and Takahashi et al. (2009) detailed two dimensional local MHD simulations of the magnetic loops. These follow-up works offer further supports for the magnetic flotation picture of F06.

In the magnetic flotation, the floated gas falls down to the galactic plane along the loop by the stellar gravity, and then collides with the nuclear gas disk. If the falling speed exceeds the sound speed, shocks must occur there, leading to violent gas motion with enhanced density and kinetic temperature by compression and heating by the shocks. This is a conversion of the magnetic energy into the kinetic and thermal energy of the gas, and the magnetic flotation may provide a unified interpretation of physical conditions and kinematics of the central molecular gas. In order to test this scenario, it is important to reveal the distribution of temperature and density in the loop, in particular, in the foot points.

In this paper, we present and discuss the results of observations in six rotational tran-

sitions of ^{12}CO ($J=1-0$, $3-2$, $4-3$, $7-6$), ^{13}CO ($J=1-0$) and C^{18}O ($J=1-0$) toward two of the foot points with the ASTE, Mopra, NANTEN2 mm/sub-mm telescopes at a few pc resolution. In this paper, we adopt a distance of 8.5 kpc to the Galactic center. Details of observations are given in section 2 and the results are given in section 3. An analysis of the line radiative transfer is given in section 4 and discussion in section 5. Conclusions are given in section 6.

2. Observations

We observed ^{12}CO ($J=1-0$), ^{13}CO ($J=1-0$) and C^{18}O ($J=1-0$) emission lines with the Mopra 22 m telescope and the ^{12}CO ($J=3-2$) line with the ASTE 10m telescope. In addition we observed the ^{12}CO ($J=4-3$, $7-6$) lines with the NANTEN2 4m telescope. The ^{12}CO ($J=3-2$) observing areas were selected by using the NANTEN ^{12}CO ($J=1-0$) dataset shown in Figure 1 as a guide. We produced a complete view of the foot points of the loops in ^{12}CO ($J=3-2$) at a $40''$ grid with a $22''$ beam size. The Mopra observations were limited to a subset of the area obtained with ASTE, but covered the brightest features associated with the foot points. NANTEN2 observations were carried out toward four small regions centered on $J=3-2$ features identified in the ASTE results (see Figure 2). The details of these observations are as follows (see also Tables 1, 2 and 3).

2.1. Mopra observations

Observations of ^{12}CO ($J=1-0$), ^{13}CO ($J=1-0$), and C^{18}O ($J=1-0$) were carried out by using the 22m ATNF Mopra mm telescope in Australia, during September 2007 and August 2008. On-the-fly (OTF) mode was used, with a unit field of $4' \times 4'$ and we scanned in both longitudinal and latitudinal directions separately to minimize scanning effects. The telescope had a half-power beamwidth (HPBW) of $33''$ at 100 GHz, which corresponds to 1.4 pc. The typical system noise temperature, T_{sys} , was 500 K in the single side band (SSB). The Mopra telescope was also equipped with backend system "MOPS", providing 4096 channels across 137.5 MHz in each of the two orthogonal polarizations. The effective velocity resolution was 0.088 km s^{-1} and the velocity coverage was 360 km s^{-1} at 115 GHz. MOPS enabled simultaneous observations of ^{12}CO ($J=1-0$), ^{13}CO ($J=1-0$), and C^{18}O ($J=1-0$). The pointing accuracy was checked every 1 hour to keep within $2''$ by observations of the 3 mm SiO maser from AH Sco [R.A. (2000) = $17^{\text{h}}11^{\text{m}}17^{\text{s}}.16$, Dec. (2000) = $-32^{\circ}19'30''.72$]. The calibration from original output data onto T_{a}^* scale and the baseline fitting was done with the livedata task in AIPS++. The spectra were gridded to a $15''$ spacing, and smoothed with a $36''$ HPBW Gaussian function. We also smooth the channels in velocity to a 0.86 km s^{-1} interval for ^{12}CO ($J=1-0$) and ^{13}CO ($J=1-0$) and a 2.0 km s^{-1} for C^{18}O ($J=1-0$). The spectra were converted into a T_{mb} scale by dividing by "extended beam" efficiency 0.55 (Ladd et al. 2005). For comparison with CO ($J=1-0$) with other excitation lines, the spectra were smoothed with a $38''$ Gaussian function beam, equivalent to the beam size of NANTEN2 at 460 GHz. We finally achieved the rms noise levels in

the $^{12}\text{CO}(J=1-0)$, $^{13}\text{CO}(J=1-0)$, and $\text{C}^{18}\text{O}(J=1-0)$ spectra of 0.13 K, 0.06 K, and 0.03 K, respectively (see also Table 1).

2.2. *ASTE observations*

Observations of the $^{12}\text{CO}(J=3-2)$ line were made using the ASTE (Atacama Submillimeter Telescope Experiment) 10m sub-mm telescope of NAOJ at Pampa la bola at an altitude of 4800 m in Chile (Kohno 2005; Ezawa 2004, 2008) for 7 days in August and September 2006. The HPBW was $22''$ at 345 GHz. We used a position switching mode to cover the region shown in Figure 1, in 1399 points, with a $40''$ grid spacing. ASTE was equipped with 345 GHz SIS receiver SC 345 providing a typical system temperature of 190–300 K of 345 GHz of an elevation angle of 30–80 degrees in the double-side band (DSB). For checking the system stability and the absolute intensity calibration, M17SW [R.A. (1950) = $18^{\text{h}}17^{\text{m}}30^{\text{s}}0$, Dec. (1950) = $-16^{\circ}13'6''.0$] was observed every 2–3 hours, the absolute temperature of which was assumed to be 69.6K (Wang et al. 1994), and we adopt a beam efficiency of 0.6 at 345 GHz. The spectrometer composes four digital back-end systems (autocorrelators) with 2048 channels. The total frequency bandwidth is 512 MHz, corresponding to a velocity coverage of 450 km s^{-1} with a velocity resolution of 0.43 km s^{-1} at 345GHz. We smoothed the data in velocity to a 0.86 km s^{-1} resolution to improve the noise level and smoothed in space to a $38''$ beam size for comparison other excitation lines. The telescope pointing was measured to be accurate to within $2''$ by radio observations of Jupiter and W Aql [R.A. (2000) = $19^{\text{h}}15^{\text{m}}23^{\text{s}}21$, Dec. (2000) = $-7^{\circ}2'49''.8$]. Finally we got a the rms noise level of $\sim 0.33 \text{ K}$ in T_{mb} .

2.3. *NANTEN2 observations*

We used the NANTEN2 4m sub-mm telescope at 4800 m altitude at Pampa La Bola in Chile to observe the four regions in the foot points (Figure 2). These regions are chosen based on the results of $^{12}\text{CO}(J=3-2)$ (see Section 3). Observations of the $^{12}\text{CO}(J=4-3)$ transition at 460 GHz and the $^{12}\text{CO}(J=7-6)$ transition at 810 GHz were made in June 2006 and December 2007. The HPBW in 460 GHz and 810 GHz were measured to be $38''$ and $22''$, respectively. The telescope was equipped with a dual-channel 460/810 GHz receiver. DSB receiver noise temperatures were $\sim 250 \text{ K}$ in 460 GHz and $\sim 750 \text{ K}$ in 810 GHz. The spectrometer was an acousto-optical spectrometer (AOS) with a bandwidth of 1 GHz of 2048 channels and the velocity resolution was 0.37 km s^{-1} at 460 GHz and 0.21 km s^{-1} at 806 GHz, respectively. We used the OTF mode with the equatorial(J2000) coordinate and scanned in both RA and Dec directions for a $2' \times 2'$ unit field. Main beam efficiencies at 460 GHz and 810 GHz were 0.5 and 0.45, respectively. The raw data were calibrated into T_{a}^* scale and then converted to T_{mb} scale by dividing by the main beam efficiency. The typical rms noise fluctuations were $\sim 0.45 \text{ K}$ at 460 GHz and $\sim 0.8 \text{ K}$ at 810 GHz at a velocity resolution of 0.86 km s^{-1} . For comparison of $^{12}\text{CO}(J=7-6)$ with other lines, the spectra were smoothed to $38''$.

3. Results

3.1. Distribution of the molecular gas

Figure 2 shows the integrated intensity distribution that includes the two foot points of loops 1 and 2 (Figure 2a) and part of the top of loop1 (Figure 2b) in $^{12}\text{CO}(J=3-2)$ at a $22'' \sim 0.9$ pc resolution. The integration range in velocity is from -180 km s^{-1} to -40 km s^{-1} , and the velocity refers to the local standard of rest (LSR). The foot points are generally elongated vertically to the plane and the most prominent feature is located from $l=356.15^\circ$ to 356.25° and $b=0.8^\circ$ to 1.0° . The rest of the distribution is extended with a few local maxima, e.g., toward $(l, b)=(356.17^\circ, 0.75^\circ)$, $(356.13^\circ, 0.78^\circ)$ and $(356.25^\circ, 1.10^\circ)$. We have chosen four peaks in the foot points, A–D, and a peak in the loop top as listed in Table 3 for a multi-J transition analysis in section 4. We note the emission is stronger in the eastern half of the distribution and that the eastern boundary shows a sharp intensity decrease perhaps barely resolved with the present resolution. Figures 3a and 4a show the distributions of $^{12}\text{CO}(J=1-0)$ and $^{13}\text{CO}(J=1-0)$ in the same velocity range at a 2 pc resolution with a spatial coverage limited to the bright part of $^{12}\text{CO}(J=3-2)$ and these distributions are generally similar to the $^{12}\text{CO}(J=3-2)$ distribution. Figures 3b and 4b show the different velocity range, -70 – -10 km s^{-1} , which exhibit a "U shape" (see section 3.2).

3.2. Velocity distribution

Figures 5-7 show the $^{12}\text{CO}(J=3-2)$ velocity distribution of the foot points in two ways, i.e., position-velocity diagrams and velocity-channel distributions every 10 km s^{-1} .

Figures 5a and 5b are latitude-velocity and longitude-velocity distributions of $^{12}\text{CO}(J=3-2)$, respectively. The main part of the foot points is distributed in a velocity range from $v = -150 \text{ km s}^{-1}$ to -40 km s^{-1} in Figure 5. The nature of the weaker emission in a velocity range greater than -40 km s^{-1} has not yet been discussed in F06, while the very narrow velocity feature at -10 km s^{-1} is perhaps foreground outside the Galactic center. Examinations of line intensity ratios like that of $^{12}\text{CO}(J=3-2)$ to $(J=1-0)$ indicates that most of the emission in Figure 5 are perhaps located in the Galactic center as suggested by their high excitation properties (section 4).

The main part of the foot points consists of two components (hereafter "main components"); one is the feature in a range from -120 km s^{-1} to -50 km s^{-1} , from 356.05° to 356.28° in l and from 0.8° to 1.2° in b , and the other that from -80 km s^{-1} to -50 km s^{-1} in v , from 356.05° to 356.22° in l and 0.6° to 0.85° in b . We identify the former component as the foot point of loop 1 and the latter that of loop 2 because their latitude ranges correspond to those of the foot points on the other ends of the two loops, respectively (see Figure 1 and F06). In Figure 5a, the loop 1 foot point is seen in a latitude range over $b=0.8^\circ$ and a velocity range from -120 to -50 km s^{-1} and the loop 2 foot point below $b=0.85^\circ$ and from -90 to -40 km s^{-1} . In

Figure 5b, the loop 1 foot point is mainly seen from -120 to -70 km s^{-1} in v and from 356.15° to 356.25° in l and a secondary feature from -120 to -80 km s^{-1} in v and from 356.05° to 356.12° in l . The loop 2 foot point is from -80 to -50 km s^{-1} and from 356.07° to 356.26° in l . The foot points as a whole show a velocity gradient in the sense that velocity increases from -110 km s^{-1} to -60 km s^{-1} toward the galactic plane with an abrupt jump from -80 to -60 km s^{-1} at $b=0.8^\circ$.@

We further note that the low velocity broad feature at -30 km s^{-1} to 10 km s^{-1} are probably linked to the main components of the foot points as suggested by the connecting broad emission at $b=0.8^\circ$ and by a few additional broad emissions at $b=0.88^\circ$, 0.94° and 1.0° . This low velocity feature shall be called as the gsub component hereafter and appears to show a velocity gradient from $b=0.80^\circ$ to 0.90° in the opposite sense to that of the main components. The sub component was not recognized in the lower resolution studies by F06 or T09. Figure 6 shows the six latitude-velocity diagrams of the foot points every 0.03° in l . The main components and the sub component are clearly seen and appears linked at $b=1.0^\circ$ (a), $b=0.9^\circ$ (d) and $b=0.8^\circ$ (d,e,f). In summary, the distribution of the molecular gas show a "U shape" in the latitude-velocity diagram consisting of the main components and the sub component.

Figure 7 shows the velocity channel distributions of the main components of the two foot points in $^{12}\text{CO}(J=3-2)$. The loop 1 foot point appears in every panel from -120 to -40 km s^{-1} while the loop 2 foot point in panels from -80 to -40 km s^{-1} . We recognize the intense part delineates a U shape in the bottom of the foot points as seen in panels from -70 km s^{-1} to -10 km s^{-1} . This U shape is also seen in Figures 3b and 4b around $b=0.8^\circ$. The loop 1 foot point is intense toward peak C, while it has a secondary feature at $l=356.0^\circ$ to 356.1° and $b=0.85^\circ$ to 0.95° . Peak A is seen in two panels from -110 to -90 km s^{-1} , peak B in four panels from -80 to -40 km s^{-1} , peak C in four panels from -100 to -60 km s^{-1} and peak D in four panels from -80 to -40 km s^{-1} . We also find that there are several small peaks other than the four and some filamentary features including the one at $l=356.2^\circ$ and $b=0.95^\circ$ to 1.10° and the other at $l=356.1^\circ$ to 356.2° and $b=0.76^\circ$ to 0.80° . A general trend in Figure 7 is that the peaks A, C and D show sharp intensity decreases toward the east and south with weaker "tails" toward the north. Figure 8 shows the details of peak C where the ^{12}CO peak velocity changes by ~ 10 km s^{-1} every ~ 20 pc with a decrease of the peak intensity by a factor of 4 toward the plane. Such a trend is not clearly seen in peak B that is embedded in spatially extended emission in panel from -70 to -60 km s^{-1} .

3.3. Line intensity ratios

We show the line spectra obtained at the four peaks A–D as well as at the peak position in the loop top in Figure 9. All the spectra are smoothed to a $38''$ Gaussian beam for comparison with the $^{12}\text{CO}(J=4-3)$ profiles and are smoothed to a 0.86 km s^{-1} resolution. Only $\text{C}^{18}\text{O}(J=1-$

0) spectra were smoothed to a 2.0 km s^{-1} resolution to obtain better signal-noise ratios. The ratios between two of the lines at the five peaks are listed for major emission features in a 10 km s^{-1} velocity width as listed in Table 4. The $^{12}\text{CO}(J=1-0, 3-2, 4-3)$ and $^{13}\text{CO}(J=1-0)$ transitions are significantly detected while the $^{12}\text{CO}(J=7-6)$ transition is not detected with an upper limit of 0.76 K . The line widths of all the spectra are broad with velocity extents of more than $20\text{--}40 \text{ km s}^{-1}$.

We show three histograms of line intensity ratios in the four velocity ranges of $-140\text{--}-40 \text{ km s}^{-1}$ (white), $-40\text{--}-20 \text{ km s}^{-1}$ (red), $-20\text{--}0 \text{ km s}^{-1}$ (orange) and $0\text{--}20 \text{ km s}^{-1}$ (green) and the combinations of these velocity (black) in Figure 10. Figure 10a shows the $^{12}\text{CO}(J=3-2)/^{12}\text{CO}(J=1-0)$ ratio, $R_{3-2/1-0}$; this indicates that the loop emission is characterized by high ratios peaked at 0.6 with a range from 0.3 to 0.95 at a 90 % peak level, somewhat smaller than $R_{3-2/1-0}$ of 0.9 by Oka et al. (2007) derived in CMZ, and the local emission having narrow linewidths mostly in a range from 0 to 20 km s^{-1} is peaked at 0.2 with a 90 % range of 0.1 to 0.6. The other two show peaks near 0.6 while the $-10\text{--}0 \text{ km s}^{-1}$ component shows another peak at 0.3 similar to the local clouds. The other two histograms, the $^{12}\text{CO}(J=1-0)/^{13}\text{CO}(J=1-0)$ ratio, $R_{1-0/13}$, (Figure 10b) and $^{12}\text{CO}(J=3-2)/^{13}\text{CO}(J=1-0)$ ratio, $R_{3-2/13}$, (Figure 10c), also indicate that the loop component and the components in a range from -40 to 0 km s^{-1} show ratios distinct from the local component from 0 to 20 km s^{-1} . Figure 11 shows a histogram of the ^{12}CO optical depth estimated by taking ratio $R_{1-0/13}$ with assumption of the abundance ratio $[^{12}\text{C}]/[^{13}\text{C}] \sim 24$ (Langer & Penzias 1990). This indicates that the gas in the loops tends to show smaller optical depths peaked at around 1–2, while the local component of -20 km s^{-1} is peaked at around 3–4. This estimates is also smaller than that of $\sim 3\text{--}10$ in the CMZ estimated by Oka et al. (1998). We summarize that the loop component is best characterized by high excitation conditions as indicated by the high ratio of the $^{12}\text{CO}(J=3-2)$ to $(J=1-0)$ line intensities and smaller ^{12}CO optical depth.

Figures 12 and 13 show the distributions of the ratio $R_{3-2/1-0}$ in velocity channel distributions and latitude-velocity diagrams, respectively. Generally speaking, the ratio is correlated with the $^{12}\text{CO}(J=3-2)$ intensity and the ratio becomes higher than 0.7 when the $^{12}\text{CO}(J=3-2)$ intensity is higher than $\sim 44 \text{ K km s}^{-1}$. The most notable enhanced ratio, corresponding to peak B, is found at $(l, b) \sim (356.18^\circ, 0.92^\circ)$ for $v=-80\text{--}-10 \text{ km s}^{-1}$, where the highest ratio is around 2.0. The secondary enhancement is seen at $(l, b) \sim (356.18^\circ, 0.7^\circ\text{--}0.8^\circ)$ and $v=-80\text{--}-60$, showing a ratio around 1.0 and corresponding to peak D. Figure 13 is generally consistent with Figure 12 and shows that the most notable enhancement is found toward the broad feature at $b \sim 0.9^\circ - 0.95^\circ$. It is also notable in Figure 13 that a high ratio feature with a very narrow velocity width of $1\text{--}2 \text{ km s}^{-1}$ is seen at $\sim -80 \text{ km s}^{-1}$ with a weak velocity gradient from $b=0.85^\circ$ to 1.05° and that another similar feature at -30 km s^{-1} from $b=0.80^\circ$ to 0.95° . These narrow features are smeared out in Figure 12.

4. Data analysis

4.1. Physical properties; Clumps

We identified clumps in the following way in the $^{12}\text{CO}(J=3-2)$ integrated intensity distributions shown in Figure 2; 1) Find local peaks that have the integrated intensity stronger than half of that in peak C, because peak C show the maximum integrated intensity level in the foot point. 2) Draw a contour at two thirds of the peak integrated intensity level and identify it as a clump unless it contains other local peaks, 3) If there are other peaks inside the contour, draw another contour with interval of 10σ and find a contour which has no other peaks inside, and 4) If we find multiple peaks with an isolated contour when we perform the operation (3), we should identify these all peaks as local peaks and repeat operations (2) and (3).

In this way, we identified six clumps in the foot point. Then, we derived physical properties of the clumps. The results are summarized in Table 5. The radii of the clumps, r , are $\sim 3-6$ pc, and the intensity weighted velocity dispersions (standard deviation), ΔV , at the peak positions are $\sim 20-36$ km s $^{-1}$. We estimate the clump masses in two ways; the mass estimated from r and ΔV by assuming virial equilibrium, M_{vir} , and the mass estimated from ^{13}CO by assuming the local thermodynamic equilibrium (LTE). M_{vir} is calculated as follows by assuming uniform density distribution;

$$M_{\text{vir}} = 209 \left(\frac{r}{\text{pc}} \right) \left(\frac{\Delta V}{\text{km s}^{-1}} \right) M_{\odot} \quad (1)$$

^{13}CO column densities are calculated by assuming the LTE condition to estimate the molecular mass. The optical depth of ^{13}CO , $\tau(^{13}\text{CO})$, was calculated using following equation;

$$\tau(^{13}\text{CO}) = -\ln \left[1 - \frac{T_{\text{R}}^*(^{13}\text{CO})}{5.29 \times (J(T_{\text{ex}}) - 0.164)} \right] \quad (2)$$

where, $T_{\text{R}}^*(^{13}\text{CO})$ and T_{ex} are the radiation temperature and the excitation temperature of ^{13}CO , respectively. $J(T)$ is defined as $J(T) = 1/[\exp(5.29/T) - 1]$. $N(^{13}\text{CO})$ was estimated from:

$$N(^{13}\text{CO}) = 2.42 \times 10^{14} \frac{\tau(^{13}\text{CO}) \Delta V T_{\text{ex}}}{1 - \exp(-5.29/T_{\text{ex}})} \text{ (cm}^{-2}\text{)}. \quad (3)$$

In this study, we assume uniform T_{ex} of 40 K as discussed in the next subsection. Then, we adopt the ratio $[\text{H}_2]/[^{13}\text{CO}] = 10^{-6}$ (Lis & Goldsmith 1989) to convert $N(^{13}\text{CO})$ into $N(\text{H}_2)$. M_{CO} of each clump is estimated by using

$$M_{\text{CO}} = 2.8 m_{\text{H}} \sum [D^2 \Omega N(\text{H}_2)] M_{\odot}. \quad (4)$$

As a result, although M_{vir} is in the order of $\sim 10^5-10^6 M_{\odot}$, M_{CO} is only in the order of $10^4 M_{\odot}$. It means that the dynamical state of the molecular gas is considerably different from the virial equilibrium when the magnetic flotation is operating.

4.2. Physical properties; Temperature and Density

We applied the large velocity gradient (LVG) analysis (Goldreich & Kwan 1974; Scoville & Solomon 1974) to estimate the physical parameters of the molecular gas toward the loop foot points and the loop top by adopting a spherically symmetric uniform model having a radial velocity gradient dv/dr . We calculate level populations of ^{12}CO , ^{13}CO and C^{18}O molecular rotational states and line intensities under the assumptions. The LVG model requires three independent parameters to calculate emission line intensities; kinetic temperature, T_k , density of molecular hydrogen, $n(\text{H}_2)$, and $X/(dv/dr)$. $X/(dv/dr)$ is the abundance ratio of CO to H_2 divided by the velocity gradient in the cloud. We use the abundance ratio $[^{12}\text{C}]/[^{13}\text{C}] \sim 24$ (Langer & Penzias 1990), and $[^{16}\text{O}]/[^{18}\text{O}] \sim 250$ (Wilson & Matteucci 1992; Wilson & Rood 1994). Lis & Goldsmith (1989) estimated the molecular abundance $[^{13}\text{CO}]/[\text{H}_2]$ as 10^{-6} in the Sgr B2 molecular cloud. Since we assume a ratio $[^{12}\text{C}]/[^{13}\text{C}]$ of 24, the molecular abundance ratio $[^{12}\text{CO}]/[\text{H}_2]$ is estimated to be 2.4×10^{-5} . Although this estimate is smaller than the $[^{12}\text{CO}]/[\text{H}_2] \sim 10^{-4}$ which is used for LVG calculations in the CMZ by Martin et al. (2004) and Hüttemeister et al. (1998), our smaller estimate seems to be more appropriate for the foot point by taking into account the ^{12}CO optical depth as discussed in section 3.3. We estimate the mean velocity gradient within the foot point as $\sim 9.0 \text{ km s}^{-1} \text{ pc}^{-1}$ (Table 5) and then $X/(dv/dr)$ to be 2.7×10^{-6} for ^{12}CO .

In order to solve temperatures and densities which reproduce the observed line intensity ratio, we calculate reduced chi-square defined as below;

$$\chi^2 = \sum_{i=1}^{N-1} \sum_{j=i+1}^N \left[\frac{\{R_{\text{obs}}(i,j) - R_{\text{LVG}}(i,j)\}^2}{\sigma(i,j)^2} \right] \quad (5)$$

$$\text{Reduced } \chi^2 = \chi^2/\nu \quad (6)$$

where N is the number of transitions of the observed molecule. i and j refer to different molecular transitions, $R_{\text{obs}}(i,j)$ is the observed line intensity ratio from transition i to transition j , $R_{\text{LVG}}(i,j)$ is the ratio between transitions i and j estimated from the LVG calculation, and $\sigma(i,j)$ is standard deviation of $R_{\text{obs}}(i,j)$. The degree of freedom, ν , is defined as follows;

$$\nu = \binom{N}{2} - p \quad (7)$$

where p is the number of fitting parameters. The error in the observed intensity is estimated by considering the noise level of the observations and the calibration error. We assume that the error of calibration from T_a^* to T_{mb} is uniformly 10 % for all observations. Because we use the same calibration factor for the spectra obtained by Mopra, the relative calibration error have no effect when we take a ratio between intensities obtained by Mopra; i.e., $^{12}\text{CO}(J=1-0)$, $^{13}\text{CO}(J=1-0)$, $\text{C}^{18}\text{O}(J=1-0)$. In order to reduce the error, we use the average line intensities of 10 km s^{-1} except for C^{18}O , because C^{18}O has already been smoothed as discussed in section

3.3 and Figure 9 and further smoothing did not give a better noise level.

The data used here are derived from the line profiles in Figure 9 and the ratios are estimated for peaks A–D and the loop top. The five ratios are listed in Table 4. They include $R_{3-2/1-0}$ (the intensity ratio $^{12}\text{CO}(J=3-2)/^{12}\text{CO}(J=1-0)$), $R_{4-3/1-0}$ ($^{12}\text{CO}(J=4-3)/^{12}\text{CO}(J=1-0)$), $R_{7-6/1-0}$ ($^{12}\text{CO}(J=7-6)/^{12}\text{CO}(J=1-0)$), $R_{1-0/13}$ ($^{12}\text{CO}(J=1-0)/^{13}\text{CO}(J=1-0)$), and $R_{1-0/18}$ ($^{12}\text{CO}(J=1-0)/\text{C}^{18}\text{O}(J=1-0)$). The values of $R_{7-6/1-0}$ are all upper limits and most values of $R_{1-0/18}$ are also upper limits.

Figure 14 shows the loci of constant $R_{j/i}$ for the five $R_{j/i}$'s as a function of density and temperature. We find $R_{3-2/1-0}$ is sensitive to a large density range from 10^2 cm^{-3} to 10^5 cm^{-3} while $R_{4-3/1-0}$ is sensitive to higher density above 10^3 cm^{-3} . We also note that $R_{1-0/13}$ is nearly orthogonal to $R_{3-2/1-0}$ for density lower than 10^4 cm^{-3} , making the combination useful in obtaining solutions.

Figure 15 shows the example results of fitting the data obtained with a chi-square minimization approach to find the best solution of temperature and density. The -65 km s^{-1} component in peak B and the -85 km s^{-1} component in peak C are shown superposed on the five intensity ratios calculated for each component. Each locus surrounding the cross indicates the χ^2/ν of 1, 1.5 and 2, which correspond to the probability of approximately 50 %, 10 %, 1 %, respectively. The crosses denote the lowest point of χ^2/ν . We show the results for all components in Figure 16a. The two components shown in Figure 15 are also included. Each locus surrounding the cross indicates the χ^2/ν of 1.5. Another presentation of the results is found in Figure 16b for the five peaks along with the $^{12}\text{CO}(J=3-2)$ line profiles and in Table 6. Density is in a range from 10^3 to 10^4 cm^{-3} and temperature is from 30–40 K to 100 K or higher while the loop top show slightly lower values less than 30 K. For about two thirds of the analyzed data normalized chi square values are less than 1.0 indicating the fitting is fairly good. As expected in $R_{3-2/1-0}$ values in Figures 12 and 13, peak B shows the highest temperature, 60 K or higher, among the five peaks.

5. Discussion

The candidates for protostars identified by IRAS point sources are not distributed in the present regions, and the radio continuum at 10 GHz (Handa et al. 1987) gives an upper limit of 0.1 K as lowest contour level. This 10 GHz flux density is equivalent to $10^{43.45}$ FUV photons s^{-1} , corresponding to a single B3 star or a star of later spectral type (Kurtz, Churchwell & Wood 1994; Panagia 1973; Mezger & Henderson 1967). Only an ultra compact HII region (UCHII) is identified at $(l, b) \sim (356.25^\circ, 0.7^\circ)$, but it has a velocity of $+120 \text{ km s}^{-1}$ from H α recombination line observations (Caswell & Haynes 1987; Lockman 1989). So, the UCHII is not associated with the foot point. There is no indication of significant formation of massive stars and some other mechanism of heating the molecular gas is required, in particular, toward peaks B and C.

The magnetic flotation model presented by F06 is able to offer another explanation to heat the gas by shocks. F06 suggested that loops 1 and 2 are created by magnetic buoyancy driven by the Parker instability. The floated gas falls down to the Galactic plane along the magnetic loop, and the accumulated gas forms a massive cloud in the foot point of the loop. In this case, if the falling down velocity of the gas exceeds the speed of sound, shock fronts are formed in the foot point (Matsumoto et al. 1988). The magnetic field is estimated to be 150 μG in the loops under the assumption of energy equi-partition, and the velocity of the gas is estimated to be similar to the Alfven speed, $\sim 24 \text{ km s}^{-1}$ (F06).

The structure of shock waves in molecular clouds is an important subject. Draine, Roberge, & Dalgarno (1983) made such calculations including the effects of ion-neutral streaming driven by the magnetic field. They found that shock waves in molecular clouds are usually C-type shock waves, mediated by the dissipation accompanying ion-neutral streaming, and in which all of the hydrodynamic variables are continuous. In the foot point of the loops, C-type shock seems to be a viable model of shocks, because C-type shock occurs with a strong magnetic field and at a moderate shock speed. The limiting shock speed for C-type shock not dissociating H_2 molecules is estimated to be 45 km s^{-1} (Draine, Roberge, & Dalgarno 1983). The Alfven speed 24 km s^{-1} estimated by F06 is within this range and hence we adopt C-type shock as the heating mechanism in the loops.

Draine, Roberge, & Dalgarno (1983) show that the neutral gas temperature is in a range 100–1000 K for density of 10^4 cm^{-3} , B of 100 μG and shock speed of 20–40 km s^{-1} . These parameters are consistent with density of 10^3 – 10^4 cm^{-3} , magnetic field of 150 μG and a falling speed of 24 km s^{-1} (F06). Such high temperature seems to be consistent with the present estimate of temperature higher than 30–40 K, since the high temperature layer should be thin like 10^{16} – 10^{17} cm , much smaller than the current resolution, a few pc. Chieze, Pineau des Forets & Flower (1998) also presented results on shock parameters consistent with the above.

We shall here compare the present results with local MHD numerical simulations (Matsumoto et al. 1988; Takahashi et al. 2009). The distribution of the foot point is basically characterized by a U shape both in space (section 3.2 and Figures 3b, 4b and 7) and in velocity (section 3.2 and Figures 5 and 6). MHD simulations indeed indicate that the foot point between two loops becomes U shaped, consisting of the two down flows from the two loops that merges at the bottom (see e.g., Figures 4 in Takahashi et al. 2009). In velocity space, the foot point consists of the foreground and background components having a large velocity splitting in the order of the Alfven speed. It is however not so straightforward to make a detailed fitting to the observations possibly because blending of two U shaped features of each foot point may be taking place. To have a solid conclusion, we must await detailed numerical simulations of the process.

The present analysis indicates that the highest ratio in the $R_{3-2/1-0}$ is formed not to-

ward the bottom of the foot points but well above the foot points apparently separated from the strongly shocked layer in the bottom of the U shape. It is interesting to compare these results with the solar foot points for which a number of observations have been accumulated on magnetic activity.

Isobe, Tripathi & Archontis (2007) argued that anti-parallel field lines are produced in the foot point when multiple loops rose. This causes magnetic reconnection for the lower density region having higher magnetic pressure and leads to a jet-like structure that rises upward. At the same time, the field lines become vertical and anti-parallel, reducing the gas flux of the falling flow and causing up stream by bouncing at the narrow neck in the foot point. Numerical simulations in the solar case suggest that the initial condition may determine which process becomes dominant, either reconnection or bouncing. The basic physics is common to the spurs in Galactic loops as already discussed by Matsumoto et al. (1988) and Takahashi et al. (2009).

We shall make a crude estimate of energies concerned. The inside of the U shape has a width of 10 pc and a height of 20 pc, and the volume in which magnetic reconnection occurs is estimated to be $10 \text{ pc} \times 10 \text{ pc} \times 20 \text{ pc}$. If we assume that the magnetic field of $150 \mu\text{G}$, then the energy of magnetic field is estimated at $E_{B\text{in}} \sim 7 \times 10^{50}$ ergs, which is almost similar to the magnetic energy of $\sim 10^{51}$ ergs for a single loop given by Machida et al. (2009). This energy divided by the typical time scale around 1 Myrs yields the maximum available power of the reconnection, $\sim 2 \times 10^{37} \text{ erg s}^{-1}$. The cooling power of the warm and low density molecular gas is estimated to be $\sim 5 \times 10^{36} \text{ erg s}^{-1}$ for kinetic temperature of 40 K (Goldsmith & Langer 1978), and corresponds to 25 % of the maximum power. We therefore conclude that the reconnection offers a viable idea to explain the warm gas, while obviously we require more detailed model simulations to reach a firm conclusion on the physical process related to the heating mechanism.

6. Conclusions

We have made detailed high-resolution observations of the foot points of the molecular loops, loop 1 and 2, discovered by Fukui et al. (2006) in six rotational transitions of the interstellar CO molecule. The main conclusions are summarized below;

1) The foot points have sharp intensity gradients toward the south and east, as is consistent with the shock formation at the bottom of the foot points. The foot point of loop 1 is mainly distributed above $b \sim 0.8^\circ$ in a velocity range from -130 km s^{-1} to 10 km s^{-1} and that of loop 2 below $b \sim 0.8^\circ$ in a velocity range from -0 km s^{-1} to -10 km s^{-1} . The foot points have several major peaks having 10^4 – $10^5 M_\odot$ for each. The foot points are characterized by a U shape both in space and velocity. We suggest that the U shape may be formed by merging of two down flows between two loops as derived in MHD numerical simulations.

2) Toward five selected peaks of $^{12}\text{CO}(J=3-2)$ including the loop top, we have carried out a multi-line LVG analysis of line radiation transfer and derived molecular temperature and density. The four peaks in the foot point show rather high temperatures of 30–40 K, slightly

higher than that in the loop top less than 30 K, and density of 10^3 cm^{-3} to 10^4 cm^{-3} . Among the four peaks, the peak toward the central region of the foot point show highest temperature of 60 K or more.

3) We compared the results with calculations of C-shock condition by Draine, Roberge, & Dalgarno (1983) and find that the derived temperature and density are roughly consistent with theoretical estimates for magnetic field around $100 \mu\text{G}$ for a beam dilution of $\sim 10^{-2}$, suggesting that the shock heating is a viable explanation for the high temperature over the foot point. In addition, by comparing theoretical works on the solar activity, we argue that the warmest region in the central part of the foot point may be additionally heated up either by magnetic reconnection or by upward flowing gas bounced by the narrow neck in the foot point.

We thank the all members of the NANTEN2 consortium, ASTE team, and Mopra staff for the operation and persistent efforts to improve the telescopes.

The Mopra telescope is funded by the Commonwealth of Australia as a National Facility managed by CSIRO as part of the Australia Telescope. The ASTE project is driven by Nobeyama Radio Observatory (NRO), a division of National Astronomical Observatory of Japan (NAOJ), in collaboration with University of Chile, and Japanese institutes including University of Tokyo, Nagoya University, Osaka Prefecture University, Ibaraki University, and Hokkaido University. Observations with ASTE were in part carried out remotely from Japan by using NTT's GEMnet2 and its partner R&E (Research and Education) networks, which are based on AccessNova collaboration of University of Chile, NTT Laboratories, and NAOJ. NANTEN2 project is based on a mutual agreement between Nagoya University and the University of Chile and includes member universities, Nagoya, Osaka Prefecture, Cologne, Bonn, Seoul National, Chile, New South Wales, Macquarie, Sydney and Zurich. @

This work is financially supported in part by a Grant-in-Aid for Scientific Research (KAKENHI) from the Ministry of Education, Culture, Sports, Science and Technology of Japan (Nos. 15071203 and 18026004) and from JSPS (Nos. 14102003, 20244014, and 18684003). This work is also financially supported in part by core-to-core program of a Grant-in-Aid for Scientific Research from the Ministry of Education, Culture, Sports, Science and Technology of Japan (No. 17004).

References

- Bania, T. M. 1977, *ApJ*, 216, 381
- Bitran, M., Alvarez, H., Bronfman, L., May, J., & Thaddeus, P. 1997, *A&AS*, 125, 99
- Caswell, J. L., Haynes, R. F. 1987, *A&A*, 171, 261
- Chieze, J. P., Pineau des Forets, G. & Flower, D. R. 1998, *Royal Astronomical Society, Monthly Notices*, 295, 672C
- Draine, B. T. 1980, *ApJ*, 241, 1021
- Draine, B. T., Roberge, W. G. & Dalgarno, A. 1983, *ApJ*, 264, 485
- Ezawa, H., Kawabe, R., Kohno, K. and Yamamoto, S. 2004, *Proc. SPIE*, 5489, 763
- Ezawa, H., et al. 2008, *Proc. SPIE*, 7012, 701208
- Fujishita, M. et al. 2009, *PASJ*, 61
- Fukui, Y., Iguchi, T., Kaifu, N., Chikada, Y., Morimoto, M., Nagane, K., Miyazawa, W. & Miyaji, T. 1977, *PASJ*, 29, 643D
- Fukui, Y., et al. 2006, *Science*, 314, 106
- Glodreich, P. & Kwan, J. 1974, *ApJ*, 189, 441
- Glodsmith, P. F. & Langer, W. D. 1978, *ApJ*, 222, 881
- Güsten, R., & Henkel, C. 1983, *A&A*, 136-145
- Güsten, R., & Philipp, S. D. 2004, in *Proc. the Fourth Cologne-Bonn-Zermatt Symposium* ed. S. Pfalzner, C. Kramer, C. Staubmeier, A. Heithausen (Heidelberg: Springer), 253
- Handa, T., Sofue, Y., Nakai, N., Hirabayashi, H. & Inoue, M. 1987, */pasj*, 39, 709
- Hüttemeister, S., Wilson, T. L., Bania, T. M. & Martín-Pintado, J. 1993, *A&A*, 280, 255
- Hüttemeister, S., Dahmen, G., Mauersberger, R., Wilson, T. L. & Martín-Pintado, J. 1998, *A&A*, 334, 646
- Isobe, H., Tripathi, D. & Archontis, V. 2007, *ApJ*, 567L, 53
- Kurtz, S., Churchwell, E. & Wood, D. O. S. 1994, *ApJS*, 91, 659
- Kohno, K. 2005, *ASP Conference series*, 344, 242
- Langer, W. D. & Penzias, A. A. 1990, *ApJ*, 357, 477
- Lis, D. C., & Goldsmith, P. F. 1989, *ApJ*, 337, 704
- Ladd, N., Purcell, C., Wong, T. & Robertson, S. 2005, *PASA*, 22, 62
- Lockman, F. J. 1989, *ApJS*, 71, 469L
- Machida, M. et al. 2009, *PASJ*, 61, 441
- Martin, C. L., Walsh, W. M., Xiao, K., Lane, A. P., Walker, C. K. & Stark, A. A. 2004, *ApJS*, 150, 239
- Matsumoto, R., Horiuchi, T., Shibata, K. & Hanawa, T. 1988, *PASJ*, 40, 171
- Mezger, P. G. & Henderson, A. P. 1967, *ApJ*, 147, 471
- Morris, M., & Serabyn, E. 1996, *ARA&A*, 34, 645
- Nagai, M., Tanaka, K., Kamegai, K. & Oka, T. 2007, *PASJ*, 59, 25
- Oka, T., Geballe, T. R., Goto, M., Usuda, T. & McCall, B. J. 2005, *ApJ*, 632, 882
- Oka, T., Nagai, M., Kamegai, K., Tanaka, K. & Kuboi, N. 2007, *PASJ*, 59, 15
- Oka, T., Hasegawa, T., Hayashi, M., Handa, T., & Sakamoto, S. 1998, *ApJ*, 493, 730
- Panagia, N. 1973, *AJ*, 78, 929

- Parker, E. N. 1966, ApJ, 145, 811
- Rodríguez-Fernández, N. J., Martín-Pintado, J., Fuente, A., de Vicente, P., Wilson, T. L. & Hüttemeister, S. 2001, A&A, 365, 174
- Scoville, N, Z., & Solomon, P. M. 1974, ApJ, 187, L67
- Scoville, N. Z., Solomon, P. M., & Penzias, A. A. 1975, ApJ, 201, 352
- Takahashi, K. et al. 2009, PASJ, 61
- Torii, K. et al. 2009, submitted to PASJ
- Tsuboi, M., Handa, T. & Ukita, N. 1999, ApJS, 120, 1
- Wang, Y., Jaffe, D. T., Graf, U. U. & Evans, N. J.,II 1994, ApJS, 95, 503
- Wilson, T. L. & Matteucci, F. 1992, A&A Rev., 4, 1
- Wilson, T. L. & Rood, R. 1994, ARA&A, 32, 191

Table 1: Observed lines

transition	frequency (GHz)	beamsize ($''$)	observing mode	noise r.m.s. (K)	telescope
$^{12}\text{C}^{16}\text{O}(J=1-0)$	115.27120	33	On the Fly	0.13	Mopra
$^{13}\text{C}^{16}\text{O}(J=1-0)$	110.20137	33	On the Fly	0.06	Mopra
$^{12}\text{C}^{18}\text{O}(J=1-0)$	109.78218	33	On the Fly	0.03	Mopra
$^{12}\text{C}^{16}\text{O}(J=3-2)$	345.79599	22	Position Switching	0.33	ASTE
$^{12}\text{C}^{16}\text{O}(J=4-3)$	461.04077	38	On the Fly	0.60	NANTEN2
$^{12}\text{C}^{16}\text{O}(J=7-6)$	806.65181	22	On the Fly	0.76	NANTEN2

Table 2: Observed areas of position-switch observaions

transition	coord.	observed area	grid ($''$)	N_{point}	comment
$^{12}\text{CO}(J=3-2)$	galactic	$(356.033^\circ, 0.633) - (356.267^\circ, 0.811^\circ)$	40	1399	foot point
		$(356.267^\circ, 0.822^\circ) - (356.300^\circ, 1.267^\circ)$			
	galactic	$(356.462^\circ, 1.191^\circ) - (356.591^\circ, 1.492)$	40	2336	top

Note. - Column (2) : Coordinate system of observations. Column (4) : Grid intervals of observations.

Column (5) : Number of total observed points.

Table 3: Observed areas of On-the-fly observations

transition	coord.	reference position	map size ($'$)	grid ($''$)	N_{map}	comment
$^{12}\text{CO}, ^{13}\text{CO}$ and $\text{C}^{18}\text{O}(J=1-0)$	galactic	$356.222^\circ, 0.845^\circ$	3 - 4	15	11	foot point
		$356.556^\circ, 1.333^\circ$	2	15	1	top
$^{12}\text{CO}(J=4-3)$ $^{12}\text{CO}(J=7-6)$	Equatorial(J2000)	$17^{\text{h}}31^{\text{m}}54^{\text{s}}58, -31^\circ08'13''76$	2	15	1	top
		$17^{\text{h}}32^{\text{m}}03^{\text{s}}68, -31^\circ30'55''44$	2	15	1	peak A
		$17^{\text{h}}32^{\text{m}}30^{\text{s}}36, -31^\circ40'04''02$	2	15	1	peak B
		$17^{\text{h}}32^{\text{m}}58^{\text{s}}84, -31^\circ40'59''49$	2	10	1	peak C
		$17^{\text{h}}33^{\text{m}}22^{\text{s}}07, -31^\circ47'51''85$	2	15	1	peak D

Note. - Column (2) : Coordinate system of observations. Column (4) : Size of the unit square of OTF scan.

Column (5) : Grid intervals of the out put data. Column (6) : Number of maps that were observed with each reference position.

Table 4: Intnsity ratio at peak positions

Peak	V _{LSR} range (km s ⁻¹)	Line ratio				
		R _{3-2/1-0}	R _{4-3/1-0}	R _{7-6/1-0}	R _{1-0/13}	R _{1-0/18}
A	-110	1.00	0.69	0.21 [†]	10.68	110.34 [‡]
	-100	0.97	0.70	0.12 [†]	9.77	111.62 [‡]
	-90	0.76	0.50	0.16 [†]	9.51	149.01 [‡]
	-80	0.60	0.30	0.29 [†]	12.00	80.00 [‡]
	-58	0.77	0.37	0.29 [†]	11.57	81.22 [‡]
B	-105	0.58	0.23	0.29 [†]	15.93	79.66 [‡]
	-95	0.79	0.28	0.15 [†]	13.19	158.33 [‡]
	-85	0.91	0.47	0.11 [†]	14.29	164.87
	-75	1.29	0.71	0.15 [†]	12.32	151.97 [‡]
	-65	1.31	0.89	0.13 [†]	16.42	180.65 [‡]
	-55	2.00	1.32	0.26 [†]	17.13	91.29 [‡]
	-45	2.23	1.66	0.80 [†]	10.36	29.00 [‡]
	-35	1.84	0.82	0.26 [†]	17.13	91.29 [‡]
	-25	1.65	1.21	0.46 [†]	7.6	50.67 [‡]
	-15	1.39	0.98	0.28 [†]	6.89	82.67 [‡]
	-5	0.79	0.52	0.13 [†]	12.07	181.03 [‡]
C	-95	0.70	0.50	0.08 [†]	14.13	141.27 [‡]
	-85	0.93	0.77	0.07 [†]	10.93	95.09
	-75	0.92	0.74	0.09 [†]	11.74	91.33
	-65	0.83	0.60	0.10 [†]	12.50	115.39 [‡]
	-55	0.60	0.35	0.13 [†]	12.71	178.00 [‡]
	-45	0.41	0.21	0.16 [†]	11.71	148.38 [‡]
D	-68	0.88	0.61	0.11 [†]	13.22	146.89 [‡]
	-58	0.98	0.74	0.07 [†]	10.60	92.98
	-48	0.88	0.59	0.13 [†]	11.53	180.67 [‡]
	-38	0.37	0.28	0.25 [†]	13.85	92.33 [‡]
TOP	-80	0.41	0.30	0.21 [†]	9.85	37.22 [‡]
	-70	0.58	0.47	0.15 [†]	9.66	53.39 [‡]
	-60	0.71	0.65	0.11 [†]	9.03	69.56 [‡]

[†] These values are upper limit because a emission wasn't detected over 3 σ noise level.

[‡] These values are lower limit because a emission wasn't detected over 3 σ noise level.

Note. - Column (2) : Center velocity of averaging range. Averaging interval is 10 km s⁻¹. Column (3-7) : Intensity ratio. R_{3-2/1-0}, R_{4-3/1-0}, R_{7-6/1-0}, R_{1-0/13} and R_{1-0/18} stand for the ratio of ¹²CO(*J*=3-2)/¹²CO(*J*=1-0), ¹²CO(*J*=4-3)/¹²CO(*J*=1-0), ¹²CO(*J*=7-6)/¹²CO(*J*=1-0), ¹²CO(*J*=1-0)/¹³CO(*J*=1-0) and ¹²CO(*J*=1-0)/C¹⁸O(*J*=1-0), respectively.

Table 5: Physical properties of the clumps.

l	b	ΔV	r	M_{vir}	M_{CO}	comment
($^{\circ}$)	($^{\circ}$)	(km s $^{-1}$)	(pc)	($\times 10^4 M_{\odot}$)	($\times 10^4 M_{\odot}$)	
356.124	0.780	26.0	4.6	65.0	2.5	
356.149	0.913	30.4	2.9	56.0	1.4	peak B
356.174	0.708	19.2	2.8	21.6	1.2	peak D
356.187	0.988	33.1	2.4	55.0	0.8	
356.220	0.838	36.0	5.9	159.8	7.4	peak C
356.254	1.113	38.2	3.9	118.9	3.0	peak A

Note. - Column (1, 2) : Peak position of the clump. Column (3) : Intensity weighted standard deviation of the velocity dispersion. Column (4) : Radius of the clumps. Column (5) : Clump mass derived with assumption of Virial equilibrium. $M_{\text{vir}} = 209r(\Delta V)^2$. Column (6) : Clump mass derived by using $^{13}\text{CO}(J=1-0)$ with LTE assumption.

Table 6: LVG results for $X(\text{CO})/(\text{dv}/\text{dr}) = 2.7 \times 10^{-6}$.

Peak	V_{LSR} (km s $^{-1}$)	$T_{\text{n(H}_2\text{)}} \text{ (cm}^{-3}\text{)}$		$T_{\text{k}} \text{ (K)}$		min. χ^2/ν
		$\chi^2/\nu < 1.5$	min. χ^2/ν	$\chi^2/\nu < 10$	min. χ^2/ν	
A	-110	$10^{3.6} - 10^{4.4}$	$10^{3.9}$	29 - 50	35	0.34
	-100	$10^{3.8} - 10^{4.2}$	$10^{4.0}$	30 - 41	34	0.73
	-90	$10^{3.7} - 10^{3.9}$	$10^{3.8}$	25 - 30	27	0.93
	-80	$10^{2.9} - 10^{3.8}$	$10^{3.5}$	20 - 108	28	0.34
	-58	$10^{3.1} - 10^{3.9}$	$10^{3.6}$	23 - 79	30	0.26
B	-105	$10^{2.3} - 10^{3.6}$	$10^{3.2}$	> 23	44	0.28
	-95	$10^{3.2} - 10^{3.6}$	$10^{3.4}$	29 - 55	36	0.71
	-85	$10^{3.3} - 10^{3.7}$	$10^{3.5}$	36 - 63	44	0.53
	-75	$10^{3.6} - 10^{3.9}$	$10^{3.7}$	40 - 52	45	1.15
	-65	$10^{3.2} - 10^{4.0}$	$10^{3.7}$	49 - 175	63	0.25
	-55	$10^{3.1} - 10^{4.1}$	$10^{3.6}$	> 63	103	0.37
	-45	$10^{3.1} - 10^{4.8}$	$10^{4.0}$	> 51	82	0.64
	-35	—	—	—	—	1.83
	-25	$10^{4.1} - 10^{4.5}$	$10^{4.3}$	41 - 59	49	1.23
	-15	—	—	—	—	1.90
	-5	$10^{3.5} - 10^{3.8}$	$10^{3.7}$	31 - 40	34	0.95
C	-95	—	—	—	—	1.91
	-85	$10^{3.8} - 10^{4.1}$	$10^{3.9}$	34 - 42	37	0.61
	-75	$10^{3.7} - 10^{4.1}$	$10^{3.9}$	34 - 43	38	0.50
	-65	$10^{3.6} - 10^{3.9}$	$10^{3.7}$	33 - 42	37	0.78
	-55	$10^{3.4} - 10^{3.6}$	$10^{3.5}$	29 - 37	32	1.24
	-45	$10^{3.3} - 10^{3.4}$	$10^{3.4}$	23 - 28	25	1.34
D	-68	$10^{3.5} - 10^{3.8}$	$10^{3.7}$	35 - 48	40	0.73
	-58	$10^{3.8} - 10^{4.1}$	$10^{3.9}$	33 - 41	36	0.54
	-48	$10^{3.6} - 10^{4.0}$	$10^{3.7}$	30 - 41	34	0.52
	-38	$10^{3.0} - 10^{3.3}$	$10^{3.2}$	33 - 57	42	1.45
TOP	-80	$10^{3.4} - 10^{3.5}$	$10^{3.5}$	21 - 26	22	1.49
	-70	$10^{3.7} - 10^{3.9}$	$10^{3.8}$	22 - 26	24	1.29
	-60	$10^{3.8} - 10^{4.3}$	$10^{4.0}$	25 - 36	28	0.89

Note. - Column (3): Number density, $n(\text{H}_2) \text{ cm}^{-3}$, for that χ^2/ν is less than 1.5. (4) : Number density, $n(\text{H}_2) \text{ cm}^{-3}$, at the point that minimum χ^2/ν is found. (5) : Kinetic temperature, $T_{\text{k}} \text{ K}$, for that χ^2/ν is less than 1.5. (6) : Kinetic temperature, $T_{\text{k}} \text{ K}$, at the point that minimum χ^2/ν is found. (7) : minimum χ^2/ν

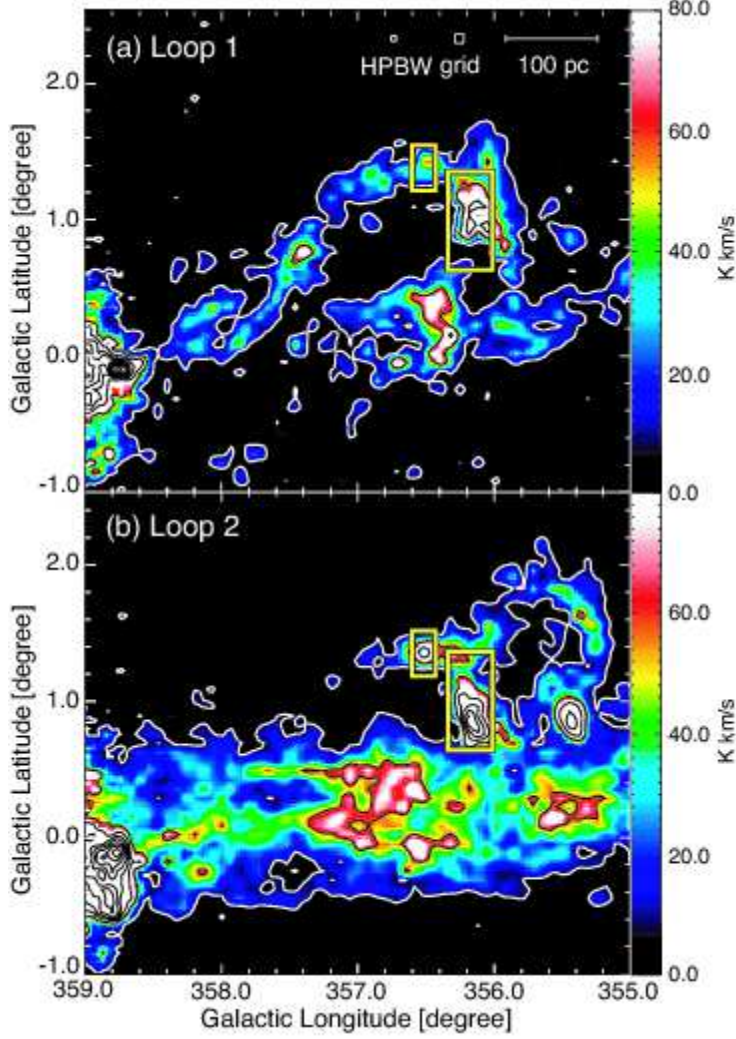


Fig. 1: Integrated intensity distributions of loops 1 and 2 in $^{12}\text{CO}(J=1-0)$ obtained by NANTEN 4m telescope. Yellow boxes in each image show the observed region in $^{12}\text{CO}(J=3-2)$ by ASTE. (a) Loop 1 : The integration range in velocity is from -180 to -90 km s^{-1} . Contours are illustrated from 7 K km s^{-1} (white) with an interval of 50 K km s^{-1} . (b) Loop 2 : The integration range in velocity is from -90 to -40 km s^{-1} . Contour levels are the same as that in (a).

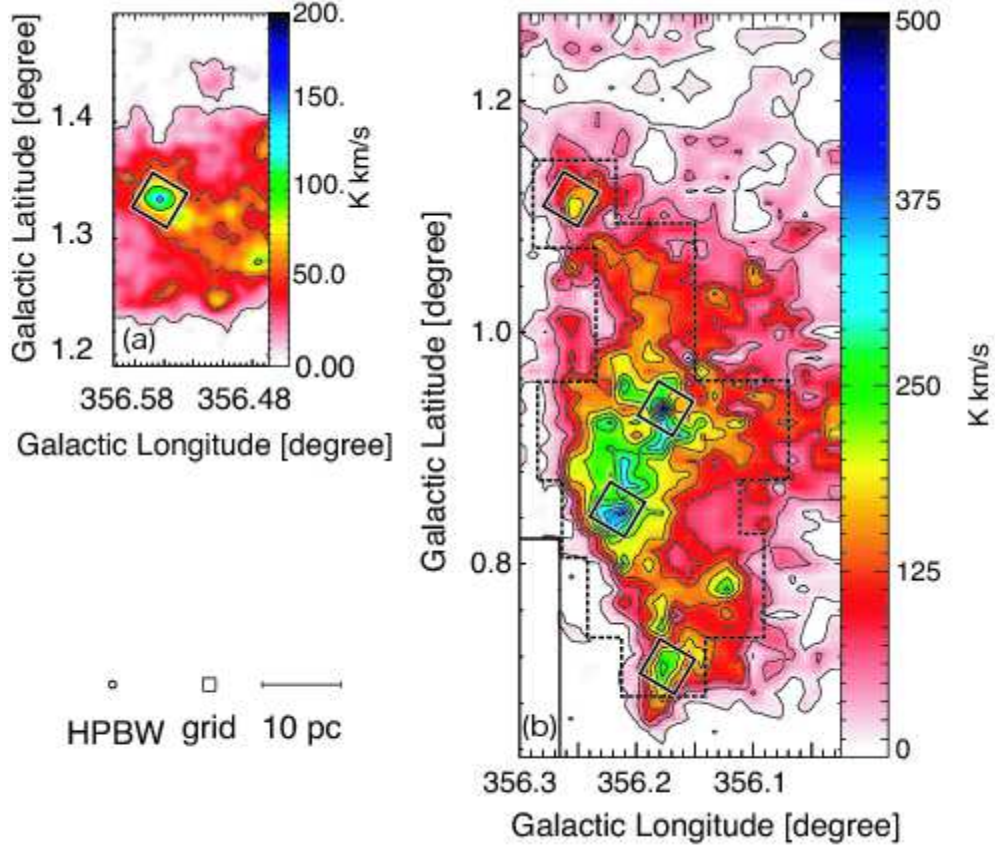


Fig. 2: Integrated intensity distributions of $^{12}\text{CO}(J=3-2)$ emissions at the top and foot point of the loops. (a) Top of the loop1. Integration range is from -180 to -40 km s^{-1} . Contours are plotted every 40 K km s^{-1} from 15 K km s^{-1} . (b) Foot point of the loops. Integration range and contour levels are the same as that in (a). The dotted box shows the observing region of $^{12}\text{CO}(J=1-0)$ emissions and $^{13}\text{CO}(J=1-0)$ emissions, that are shown in Figures 3 and 4. The small boxes show the observing regions of $^{12}\text{CO}(J=4-3, 7-6)$ emissions.

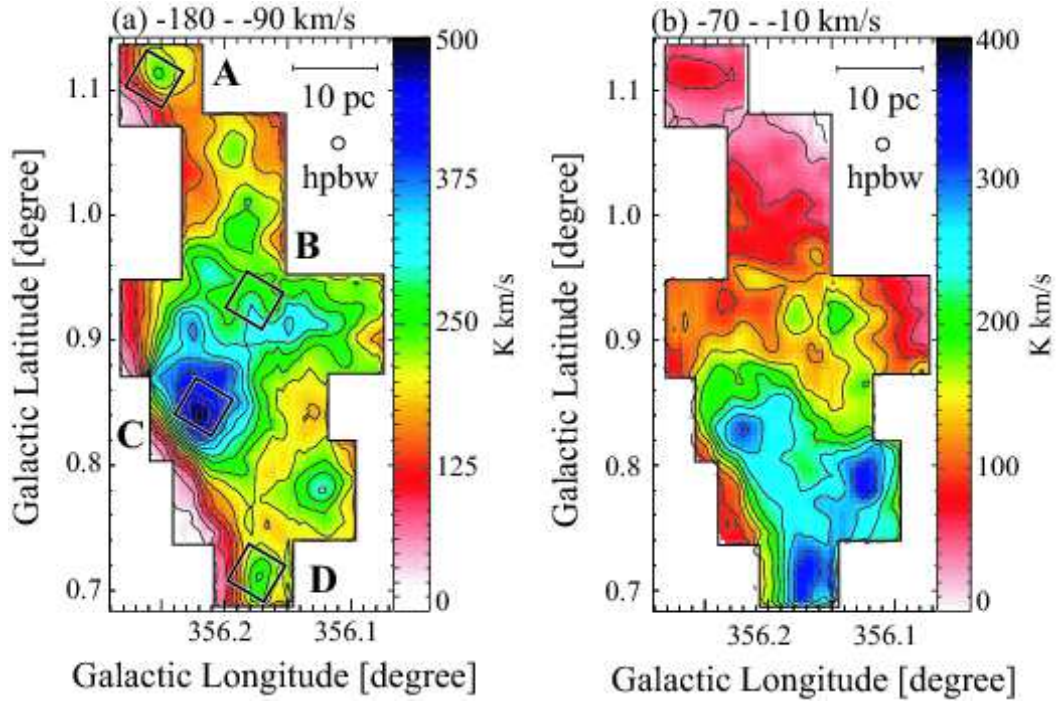


Fig. 3: Integrated intensity distribution of $^{12}\text{CO}(J=1-0)$ emissions at the foot point of the loops. Integration ranges are from -180 to -40 km s $^{-1}$ (a) and from -70 to -10 km s $^{-1}$ (b). Contours are plotted every 30 K km s $^{-1}$ from 2 K km s $^{-1}$.

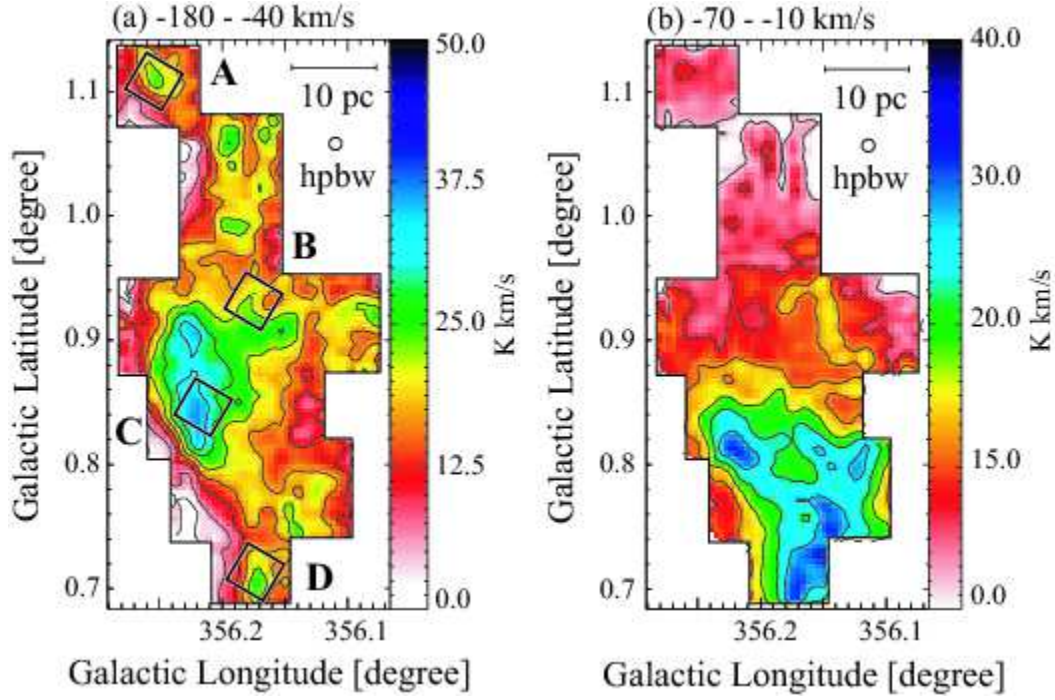


Fig. 4: Integrated intensity distribution of $^{13}\text{CO}(J=1-0)$ emissions at the foot point of the loops. Integration ranges are from -180 to -40 km s $^{-1}$ (a) and from -70 to -10 km s $^{-1}$ (b). Contours are plotted every 5 K km s $^{-1}$ from 2 K km s $^{-1}$.

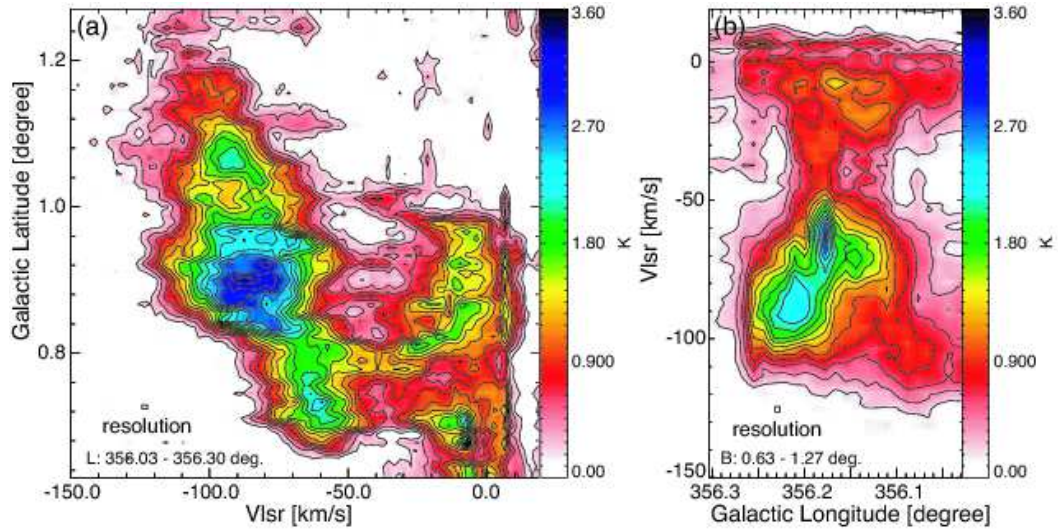


Fig. 5: (a) Velocity - galactic latitude diagram of the footpoint of the loops averaged from 356.03° to 356.27° in galactic longitude. Contours are plotted every 0.2 K. (b) Galactic longitude - velocity diagram of the footpoint of the loops averaged from 0.63° to 1.27° in galactic latitude. Contours are plotted every 0.2 K.

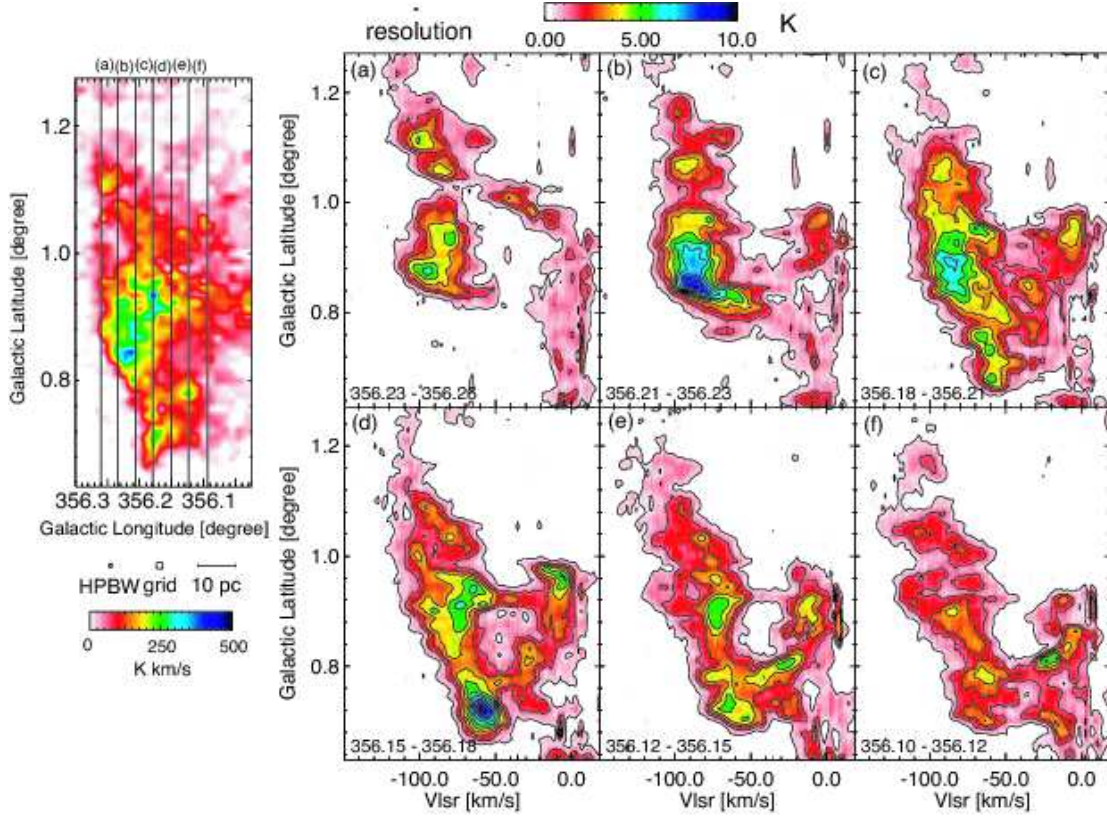


Fig. 6: (a–f) Longitude channel maps of $^{12}\text{CO}(J=3-2)$ averaged over successive $100''$ intervals. Contours are plotted every 1 K from 0.5 K. The figure in the left side is the integrated intensity distributions which is the same as the image shown in figure 2. Solid lines in the figure show the integration ranges of figures (a) – (f).

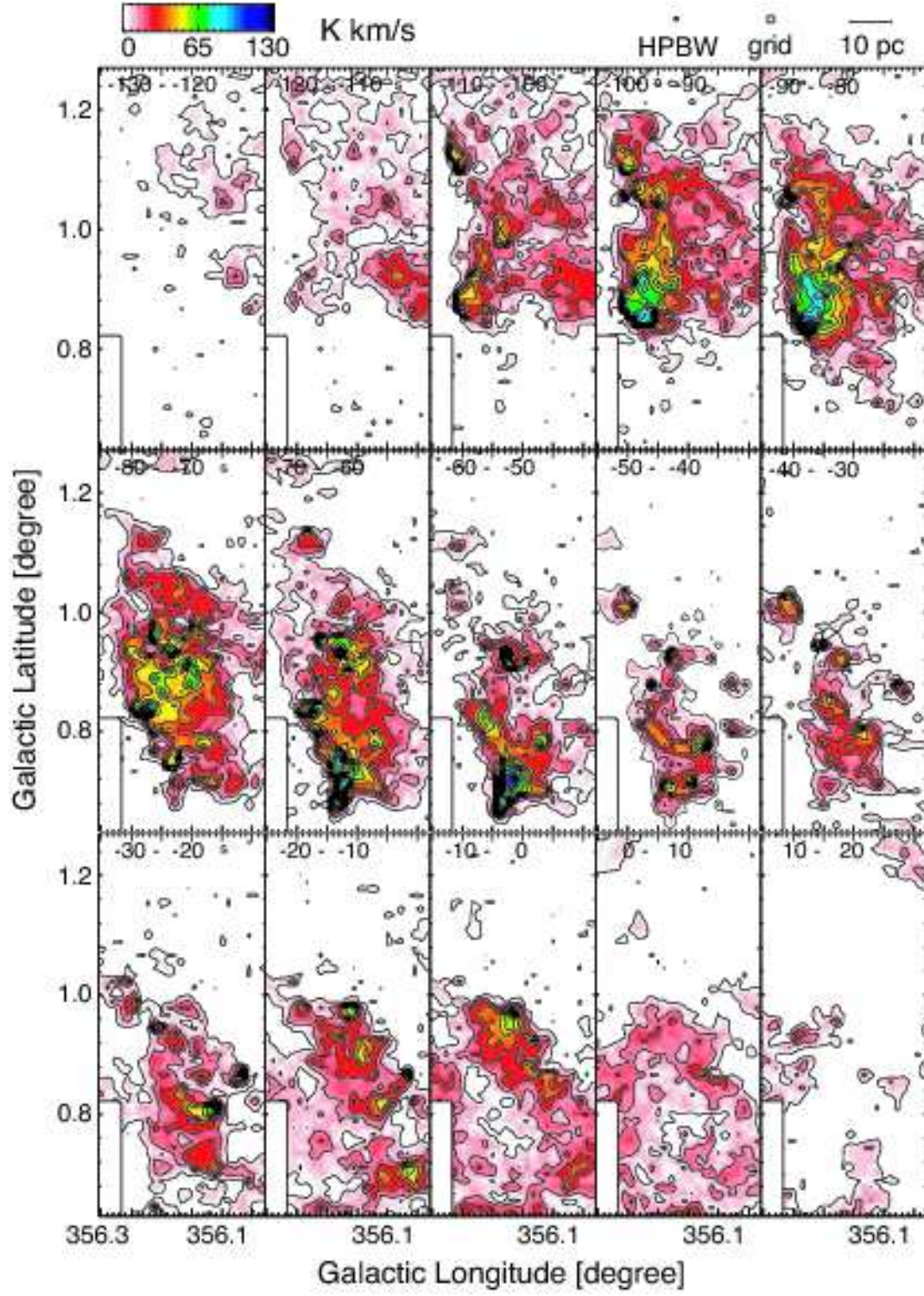


Fig. 7: Velocity channel maps of $^{12}\text{CO}(J=3-2)$ integrated over successive 10 km s^{-1} . Contours are illustrated every 10 K km s^{-1} from 4 K km s^{-1} .

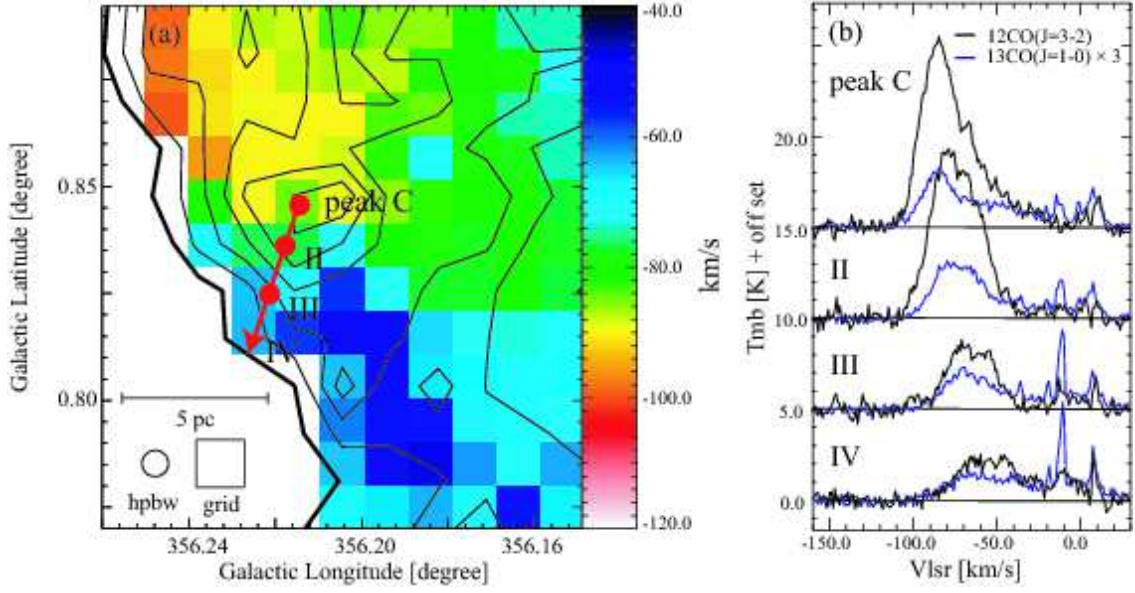


Fig. 8: (a) Peak velocity map around peak C estimated with $^{12}\text{CO}(J=3-2)$ is shown in color image. Contours show the integrated intensity levels of $^{12}\text{CO}(J=3-2)$ integrated from -140 to -40 km s^{-1} and are plotted every 60 K km s^{-1} . (b) $^{12}\text{CO}(J=3-2)$ and $^{13}\text{CO}(J=1-0)$ spectra of the four points on the red arrow in figure (a). The order of the spectra is the direction of the red arrow, from peak C to the left-bottom of the peak C.

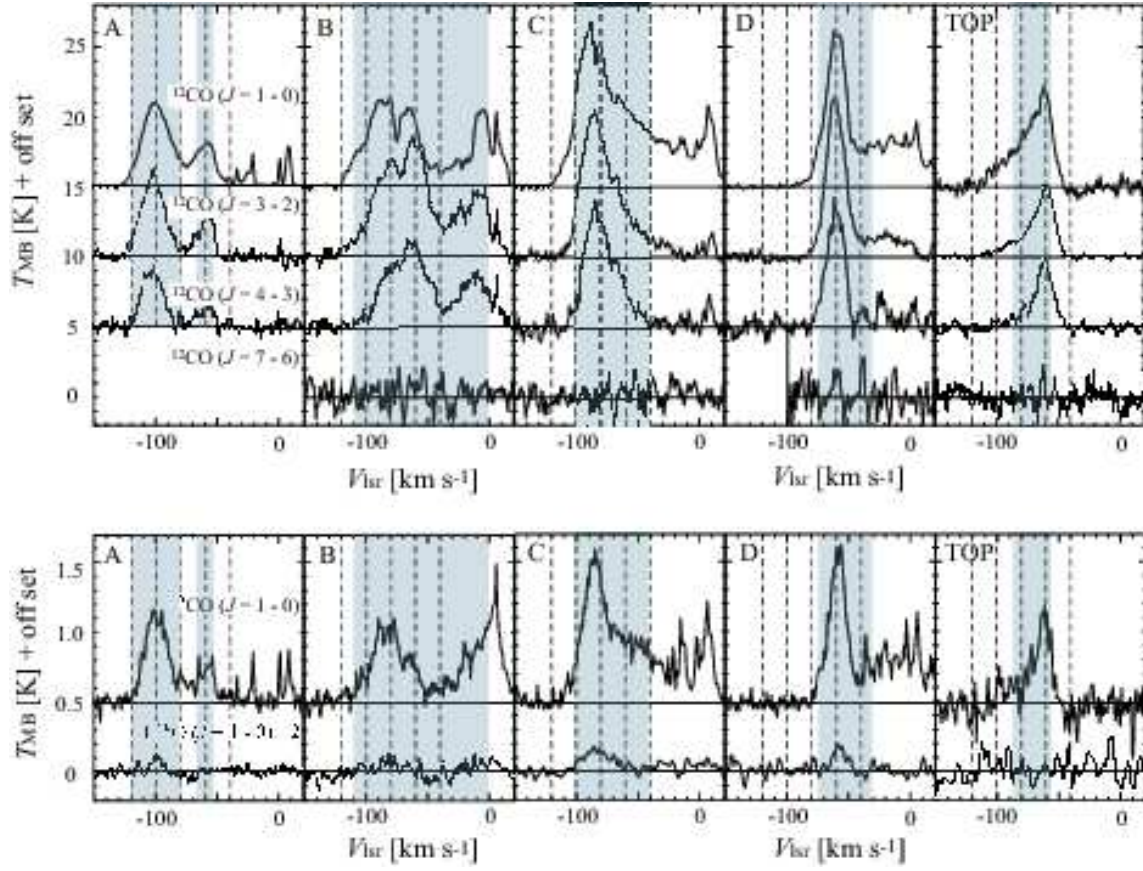


Fig. 9: Observed CO spectra in the peak of the clumps. Only $\text{C}^{18}\text{O}(J=1-0)$ spectra were doubled. The vertical dashed lines are drawn with 20 km s^{-1} intervals from -120 km s^{-1} .

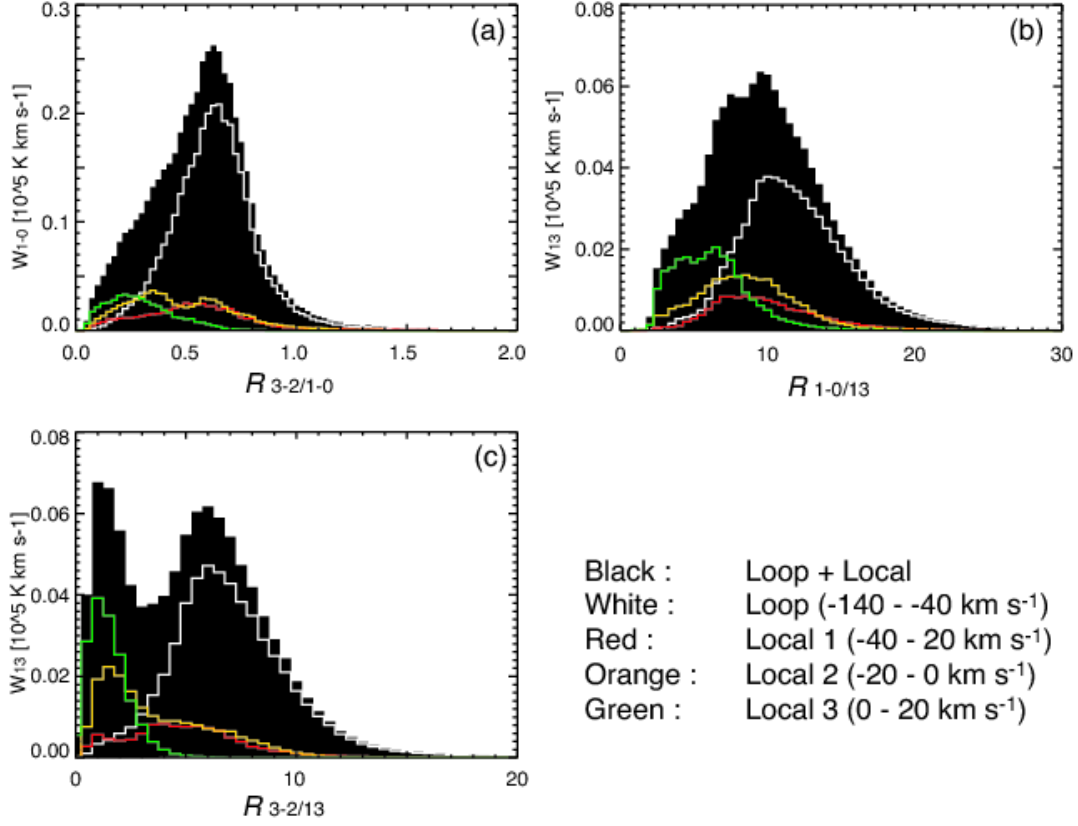


Fig. 10: Intensity weighted frequency distributions of the CO intensity ratio. The data are smoothed to a 60'' resolutions with gaussian function and smoothed to a 2 km s⁻¹ resolutions. The white lines show the contributions of the loops (-140 km s⁻¹ to -30 km s⁻¹), and the red, orange and green lines show the contributions of the local components with a interval of 20 km s⁻¹ from -40 km s⁻¹. (a) $R_{3-2/1-0} = {}^{12}\text{CO}(J=3-2)/{}^{12}\text{CO}(J=1-0)$. (b) $R_{1-0/13} = {}^{13}\text{CO}(J=1-0)/{}^{12}\text{CO}(J=1-0)$. (c) $R_{3-2/13} = {}^{13}\text{CO}(J=1-0)/{}^{12}\text{CO}(J=3-2)$.

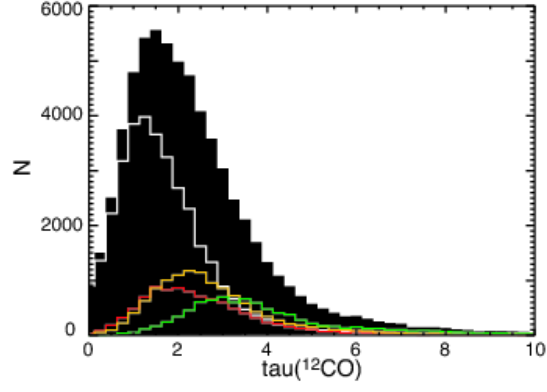


Fig. 11: Frequency distribution of the $^{12}\text{CO}(J=1-0)$ optical depth in the foot point of the loops. The data are smoothed to a 5 km s^{-1} resolutions. The white line shows the contributions of the loops (-140 km s^{-1} to -30 km s^{-1}), and the red, orange and green lines show the contributions of the local components same as Figure 10.

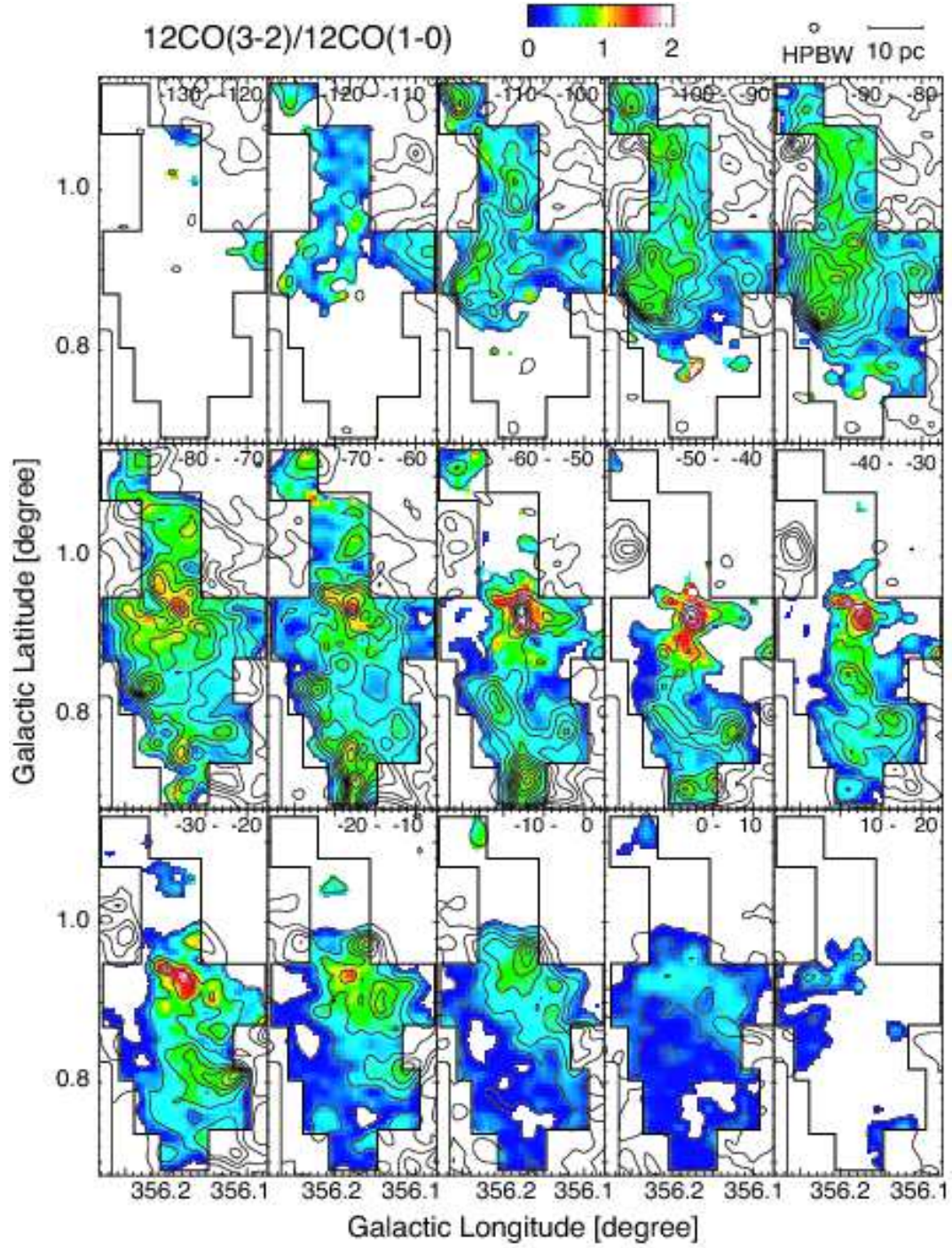


Fig. 12: Velocity channel maps of the $^{12}\text{CO}(J=3-2)/^{12}\text{CO}(J=1-0)$ intensity ratio integrated over successive 10 km s^{-1} . Contours are $^{12}\text{CO}(J=3-2)$ and illustrated every 10 K km s^{-1} from 4 K km s^{-1} .

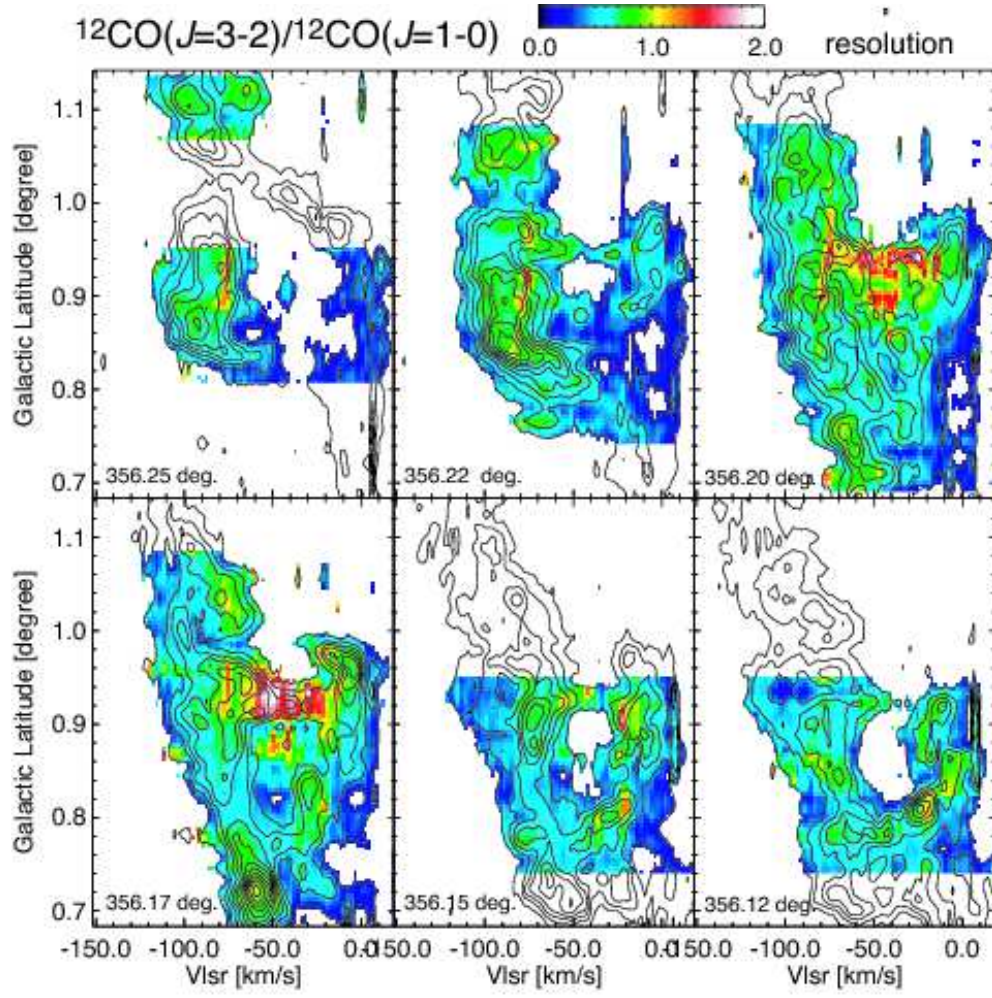


Fig. 13: Longitude channel maps of the $^{12}\text{CO}(J=3-2)/^{12}\text{CO}(J=1-0)$ intensity ratio averaged for successive $45''$ with an interval of $120''$. Contours are the averaged intensity of $^{12}\text{CO}(J=3-2)$ and are plotted every 1 K from 0.5 K.

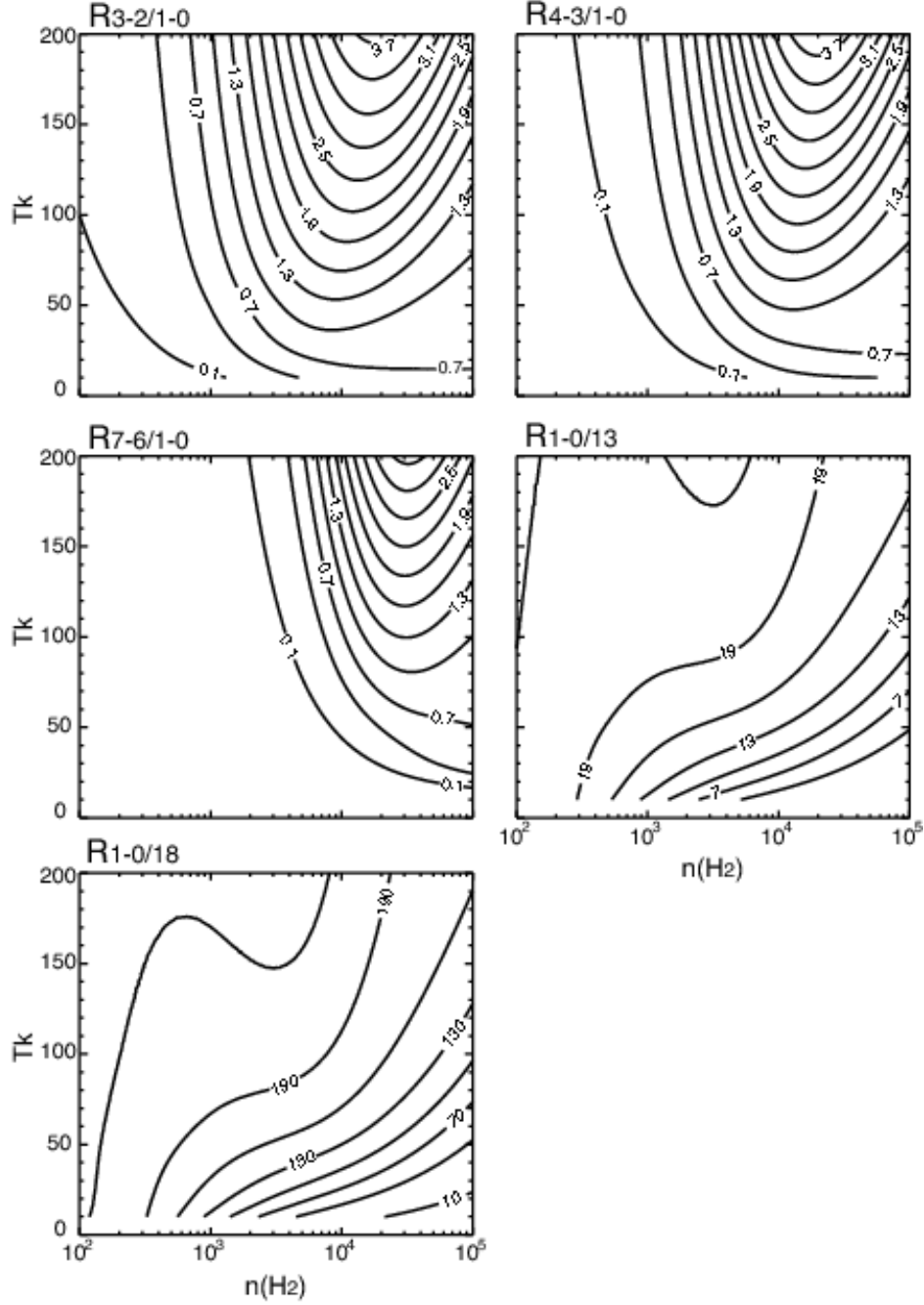


Fig. 14: Intensity ratio distributions in the density-temperature space calculated from the LVG model for $X(\text{CO})/(\text{dv}/\text{dr})$ of 2.7×10^{-6} . $R_{3-2/1-0}$, $R_{4-3/1-0}$, $R_{7-6/1-0}$, $R_{1-0/13}$ and $R_{1-0/18}$ stand for the intensity ratio of $^{12}\text{CO}(J=3-2)/^{12}\text{CO}(J=1-0)$, $^{12}\text{CO}(J=4-3)/^{12}\text{CO}(J=1-0)$, $^{12}\text{CO}(J=7-6)/^{12}\text{CO}(J=1-0)$, $^{12}\text{CO}(J=1-0)/^{13}\text{CO}(J=1-0)$ and $^{12}\text{CO}(J=1-0)/\text{C}^{18}\text{O}(J=1-0)$, respectively.

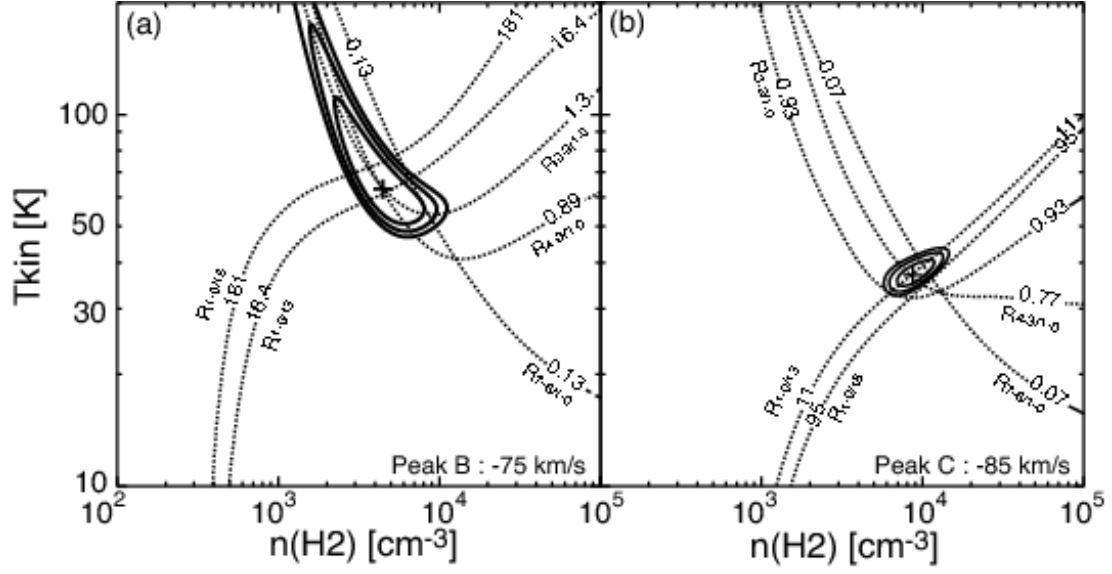


Fig. 15: LVG results of peak B (-65 km s^{-1}) and peak C (-85 km s^{-1}) for $X(\text{CO})/(\text{dv}/\text{dr})$ of 2.7×10^{-6} . Solid contours show the reduced chi-square, χ^2/ν , distributions and are plotted at the levels of 1, 1.5 and 2. The crosses show the points that the minimum χ^2/ν are found. Dotted contours show the intensity ratio; $R_{3-2/1-0}$, $R_{4-3/1-0}$, $R_{7-6/1-0}$, $R_{1-0/13}$ and $R_{1-0/18}$ stand for the intensity ratio of $^{12}\text{CO}(J=3-2)/^{12}\text{CO}(J=1-0)$, $^{12}\text{CO}(J=4-3)/^{12}\text{CO}(J=1-0)$, $^{12}\text{CO}(J=7-6)/^{12}\text{CO}(J=1-0)$, $^{12}\text{CO}(J=1-0)/^{13}\text{CO}(J=1-0)$ and $^{12}\text{CO}(J=1-0)/\text{C}^{18}\text{O}(J=1-0)$, respectively. Drawn levels of the dotted lines are the ratios at the -75 km s^{-1} point of peak B (a) and the -85 km s^{-1} point of peak C (see Table 4).

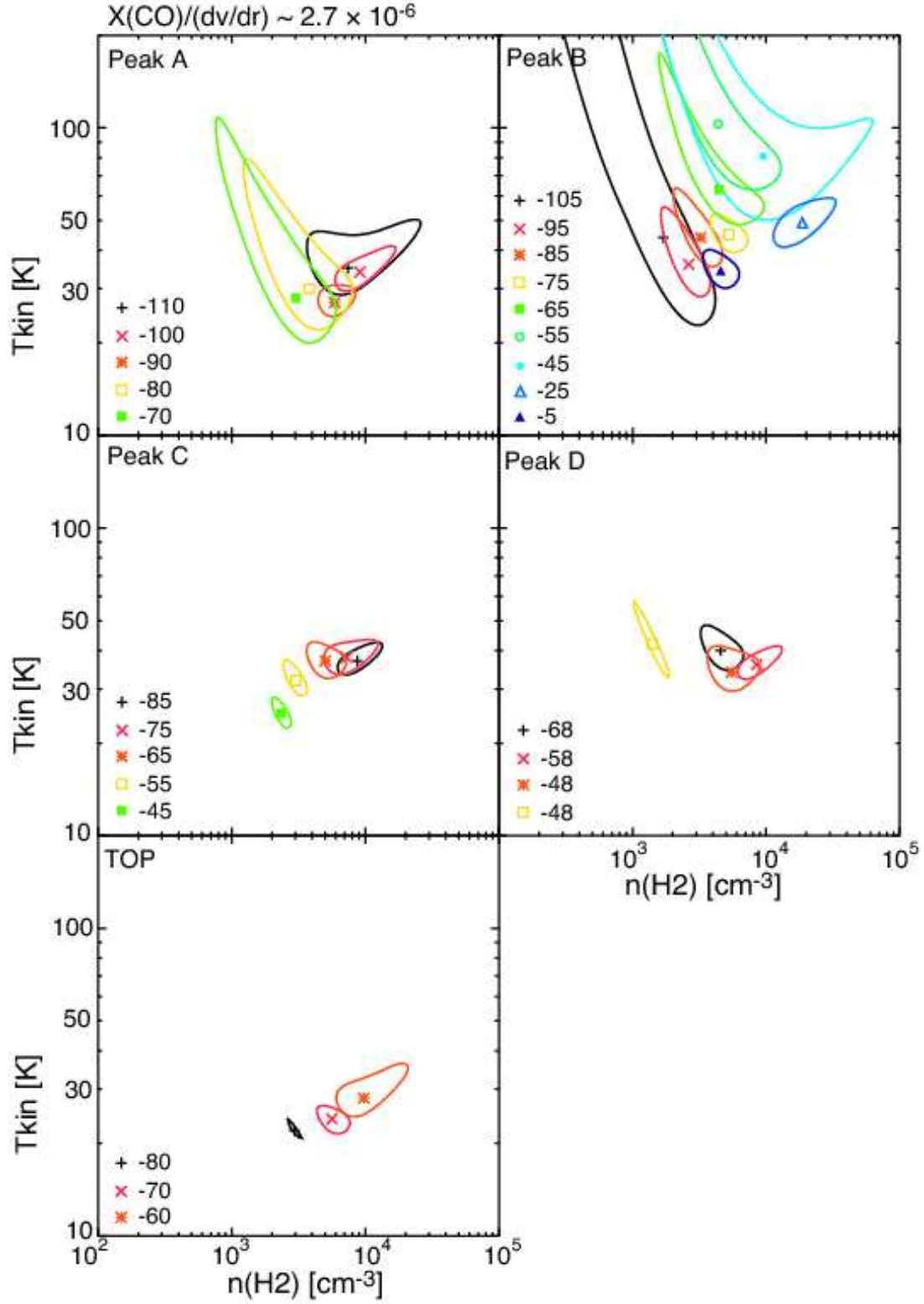


Fig. 16a: Reduced chi square, χ^2/ν , distributions for the different velocity of the clumps. Colored lines are plotted at 1.5 in all figures, and the symbols show the points that minimum χ^2/ν is found. Details are summarized in Table 6.

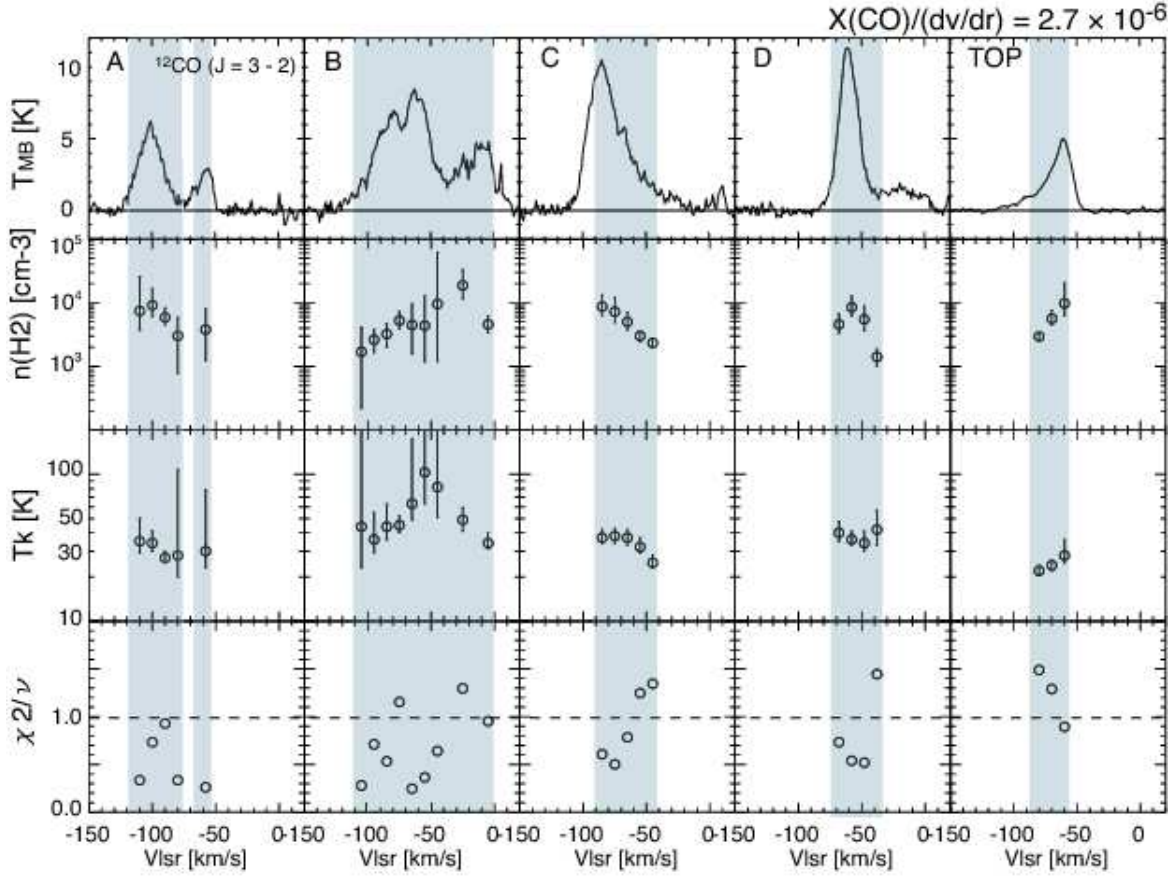


Fig. 16b: LVG results for $X(\text{CO})/(\text{dv}/\text{dr})$ of 2.7×10^{-6} for five spectra at the peaks. Horizontal axis of all figures is LST velocity. Top row shows the $^{12}\text{CO}(J=3-2)$ spectra at the peaks A - D, and the peak in the loop top. The second and third rows show the number density, $n(\text{H}_2)$ cm^{-3} and the kinetic temperature, T_k K, respectively. Circles and bars show the point that the minimum chi square, χ^2/ν , is found and the range that χ^2/ν show less than 1.5, respectively. The minimum χ^2/ν are shown in fourth row.